Non-allometric expansion and enhanced compartmentalization of Purkinje cell dendrites in the human cerebellum

Silas E. Busch[1] and Christian Hansel[1*]

[1]Department of Neurobiology and Neuroscience Institute, The University of Chicago, Chicago, IL, USA
[*]Correspondence: chansel@bsd.uchicago.edu

Abstract
Purkinje cell (PC) dendrites are optimized to integrate the vast cerebellar input array and drive the sole cortical output. PCs are classically seen as stereotypical computational units, yet mouse PCs are morphologically diverse and those with multi-branched structure can receive non-canonical climbing fiber (CF) multi-innervation that confers independent compartment-specific signaling. While otherwise uncharacterized, human PCs are universally multi-branched. Do they exceed allometry to achieve enhanced integrative capacities relative to mouse PCs? To answer this, we used several comparative histology techniques in adult human and mouse to analyze cellular morphology, parallel fiber (PF) and CF input arrangement, and regional PC demographics. Human PCs are substantially larger than previously described; they exceed allometric constraint by cortical thickness and are the largest neuron in the brain with 6-7cm total dendritic length. Unlike mouse, human PC dendrites ramify horizontally to form a multi-compartment motif that we show can receive multiple CFs. Human spines are denser (6.9 vs 4.9 spines/µm), larger (~0.36 vs 0.29µm), and include an unreported 'spine cluster' structure—features that may be congruent with enhanced PF association and amplification as human-specific adaptations. By extrapolation, human PCs may receive 500,000 to 1 million synaptic inputs compared with 30-40,000 in mouse. Collectively, human PC morphology and input arrangement is quantitatively and qualitatively distinct from rodent. Multi-branched PCs are more prevalent in posterior and lateral cerebellum, co-varying with functional boundaries, supporting the hypothesis that this morphological motif permits expanded input multiplexing and may subserve task-dependent needs for input association.

Keywords
Mouse; Dendrite Branching; Dendritic Trunk; Climbing Fiber; Parallel Fiber; Allometric Scaling; Neuron; Cerebellar cortex; Spine; Comparative Anatomy

Introduction

Being the sole output of the cerebellar cortex, Purkinje cells (PCs) perform the final step to integrate all cortical input. The dendritic arbor of each PC is the target of tens of thousands of granule cell parallel fiber (PF) axons, which deliver an expansion recoding of mossy fiber contextual input[1,2], and prediction-error signals carried by one—*or several*—climbing fiber (CF) axons from the inferior olive[3,4]. Understanding cerebellar function thus requires us to understand the process of PC dendritic integration.

PC dendrite structure and function is adapted to receive the most synaptic connections on one of the largest dendritic arbors of the central nervous system. Yet, PC dendrites appear to adapt beyond being simply large and densely innervated. Recent work has shown that PC dendrites are morphologically diverse[4–6] and their sub-branches can exhibit heterogeneous physiological excitability[7–13]. Primary dendrite morphology can influence patterns of CF innervation, in some cases permitting non-canonical CF multi-innervation in adult mice that confers independent signaling across compartments *in vivo*[4]. A study using patch clamp electrophysiology in cerebellar slices found that dendritic compartments can undergo independent plasticity[10]. Combined physiological and calcium imaging experiments in awake mice found that intrinsic and synaptic plasticity mechanisms can operate on distinct, compartment-level spatial scales to tune dendritic signaling and gate its impact on axosomatic output[14].

Morphology thus plays a critical role in shaping PC input integration. While this insight comes largely from the use of the experimentally accessible rodent cerebellum, human PCs are far more enigmatic. Very little is known about the nature of their dendrite morphology, input arrangement, or physiology. Since their illustration

by Camillo Golgi[15] and Santiago Ramón y Cajal[16], the morphology of human PC dendrites have only been analyzed occasionally and in small numbers[17–19], eluding systematic quantification. We recently developed a framework for morphological categorization and performed a comparative analysis of thousands of PCs in human and mouse[4]. We defined PCs as having either one ("Normative") or multiple primary dendrite compartments ("Split" when compartments arise from one proximally bifurcated dendrite, or "Poly" when multiple dendrites emerge directly from the soma). This approach revealed that human PCs are almost universally multi-branched whereas a plurality of mouse PCs are Normative. In mice, ~25% of multi-branched PCs received multiple functionally distinct CFs while Normative cells did not, indicating a link between primary dendrite morphology and cellular physiology. Human PC physiology, on the other hand, remains largely inaccessible, but recent work leveraged limited access to acute human cerebellar tissue and a comparative modeling approach to make important progress[20]. To further understand human PC physiology, we will require more complete data on their dendritic morphology and the arrangement of inputs such as PFs and CFs on the arbor.

Here, we provide a comprehensive quantification and comparative analysis of human and mouse PC morphology, excitatory input arrangement, and regional distribution. Our reconstructions reveal that—with dendritic lengths of 6-7cm—Purkinje cells far exceed pyramidal cells in having the largest dendritic arbor in the human brain. They also exceed the allometric constraint of cortical thickness by ramifying horizontally and increasing compartmentalization to produce an expanded multi-branched structural motif. We hypothesized that this motif would permit more input multiplexing and association. In support of this, we found that human cells have increased spine size (~0.36 vs 0.29μm diameter) and density (6.9 vs 4.9 spines/μm)—receiving upwards of 1 million inputs compared with 30-40,000 in mouse—and host a previously unreported 'spine cluster' structure not found in mouse. Co-labeling PCs (calbindin) and CFs (peripherin) confirms that non-canonical CF multi-innervation is present in adult human, as in mouse[4]. The regional prevalence of a multi-branched motif among PC populations covaries with human functional boundaries and exhibits sub-regional patches of clustered morphologies. This supports the hypothesis that a multi-branched structure can provide for enhanced input multiplexing and that this may subserve complex multimodal association and learning in posterior and lateral cerebellar regions.

Results

Human PCs are not an allometrically scaled mouse PC

We used fluorescent calbindin immunohistochemistry in fixed, unembalmed post-mortem cerebellar tissue to achieve specific and complete labeling of human PCs for cellular reconstruction (Fig. 1A; Methods). Unlike embalmed human tissue, as used previously[4] and for regional analysis below, immunolabeling of unembalmed tissue provides variable sparseness of cell labeling that is ultimately more complete and produces brighter staining that dramatically enhances the signal to noise ratio. Calbindin density in mouse tissue precludes individual cell separation, so we acheived sparse labeling via viral expression of Cre-dependent GCaMP6f (Fig. 1B; Methods). High resolution z-stack confocal scans (~0.2μm x 0.2μm x 0.5μm voxel resolution) permitted manual reconstruction and analysis of dendritic morphology (n = 5,5 cells; Fig. S1). Human PCs were selected for isolation from adjacent cells and completeness of the arbor but minor truncation (approximately <5%) was unavoidable. Occasionally branches from adjacent PCs were visible near and within the area of the dendritic arbor, but these could be reliably excluded from the manual reconstructions as they were disconnected from the cell of interest.

Human PCs were substantially (~11x) longer than in mouse, more than was previously appreciated[5,19–26] (Fig. 1C), having total dendritic lengths of 63,645±4572μm and 6,004±831um, respectively (Fig. 1D). Human PCs had 3.9x the number of total and terminal branch segments (2,750±247 vs 707±118 and 1,377±125 vs 355±59; Fig. 1E and S2A), which were produced by branching that reached nearly double the maximum and average branch order (50±5.4 vs 28±5.3 and 25±2.5 vs 14±2.6; Fig. 1F and S2B). Despite considerable morphological variation, a trend emerged wherein human primary dendrites commonly ramified parallel with the PC layer and bore numerous, often 7-8 (Fig. S2C), compartments that projected vertically toward the pial surface. This alignment rendered their abor ~4.5x wider than in mouse (644±126μm vs 143±31μm; Fig. 1G), while their molecular layer thickness—a crucial allometric variable—defined the maximal arbor height only 2.3x taller (366±58μm vs 158±22μm; Fig. 1H). Thus, human PCs attained a horizontal dimensionality with 79±42% greater width than height while mouse PCs had 6.3±31% greater height than width (Fig. 1I). Horizontal orientation was not limited to the primary dendrites. Across branching orders and somatic distances, human branches ramified at more horizontal eccentricities than in mouse (~37±24° vs 45±24°; Fig. 1J). Both human and mouse dendrite eccentricities turned upward with increased distance from the soma (~29±23°, 39±24°,42±23° among branches in proximal, intermediate, and distal compartments vs 41±24°, 43±25°, and 51±23°; Fig. 1J), a trend conserved across cells (Fig. S2D).

Emerging from a somatic compartment that is 2x the diameter (7.7x the volume) of mouse (32.8±3.07μm vs 16.5±0.78μm; Fig. S2E), human primary dendrites were 2.1x thicker (6.49±2.43μm vs 3.12±1.17μm; Fig. 1K). Human dendrites narrow nearly ten-fold as they branch (Fig. 1L) such that the spiny dendrites of both species converge on an apparently conserved thickness (~0.6-1μm; Fig. 1M and S2F). As a result, most branching orders have only ~15% the diameter of the primary dendrite in human compared with ~25% in mouse (Fig. 1N). Relatedly, 95% of human dendritic length is devoted to thin, spiny dendrites with <1.3μm diameter (the log-normal mean + 1SD of dendrite diameter across species) while that figure is 89% in the mouse (Fig. 1O).

Both species shared patterns of near-symmetric fractal branching over similar relative orders (17/50, 34% vs 10/28, 36%; Fig. S2G) and evenly distributed length (Fig. S2H). Individual branch segments were 2.3x longer on average in human and varied more in their length (24.53±18.78μm vs 9.23±5.7μm; Fig. 1P). The species difference was even greater (3x) among terminal dendritic segments (33.14±19.59μm vs 10.9±5.81μm; Fig. S2J). Also reflecting more heterogeneity in the human arbor, the rate of branch emergence in human peaked at precisely half the dendritic height while mouse PC branch segments emerged at a constant rate through roughly the middle 60% of their arbor (Fig. S2K). This pattern was also observed in the distributions of relative total dendritic length (Fig. 1Q-R) and branch number (Fig. S2L-M) across Sholl radii.

Human-specific adaptations for size and associative complexity in spine structure and number

As predominantly the sites of excitatory PF input and plasticity, dendritic spines and their morphology contribute to PC physiology. To assess this input pathway, we manually reconstructed ~4,000 spines from high resolution confocal z-stack images (~26nm x 26nm x 150nm voxel resolution) of spiny dendrite segments across molecular layer compartments of the same tissue as used above for cell reconstruction (Fig. 2A;

Methods). Dendrite sections were chosen for their isolation from nearby branches. This ensured that there was no substantial contamination of the field of view by spinous or dendritic structures from other branches. Some truncated PC dendrite and spine structures were unavoidably present, but these could be distinguished from connected and putatively connected structures when scrolling through the z-plane. Human PCs exhibited higher spine density than mouse PCs (6.81±0.77 vs 5.1±0.61spines/μm; Fig. 2B). Both species had higher densities on distal dendrites (6.32±0.62 to 7.1±0.77/μm in proximal vs distal compartments of human; 4.55±0.55 to 5.48±0.35/μm in mouse; Fig. 2C), suggesting that increased PF input density on distal compartments may be a conserved mammalian trait[27]. Combining measures of total dendritic length and spine density, we can extrapolate that a mouse PC has roughly 30-40,000 spines, consistent with recent findings[28], while a human PC has roughly 400-600,000 spines.

The elevation in human spine density was largely attributable to thin-head spines (5.37±0.82 vs 4.56±0.56/μm) and large mushroom spines (0.49±0.44 vs 0.13±0.14/μm). Thin spine density increased in distal branches of mouse (4.09±0.64 to 4.86±0.28/μm) while mushroom spine density increased in distal branches of human (0.39±0.45 to 0.7±0.59/μm). Both species had similar densities of branched spines[29–32] (0.42±0.18 vs 0.49±0.13/μm) that were elevated on distal branches (0.38±0.19 to 0.45±0.18/μm in human and 0.37±0.11 to 0.6±0.08/μm in mouse).

Head diameters of thin and mushroom spines were relatively larger in human (0.36±0.1μm vs 0.29±0.08μm; Fig. 2D). As in our cell reconstructions (Fig. S2N-O), spiny dendrite thicknesses were equivalent in both species (0.68±0.1μm vs 0.73±0.1μm; Fig. S3C), leading us to hypothesize that human spine necks may be longer to maintain a similar volume ratio between spines and the space surrounding the dendrite (see Methods). Spine necks were indeed longer on average in human (0.83±0.48μm vs 0.7±0.31μm; Fig. 2E), but the ratio of spine to surrounding volume nearly doubled from mouse to human (1.96±0.5% vs 3.73±0.92%; Fig. 2F), such that elongated necks did not compensate for elevated spine density and size in the human. Increased spine neck length and head diameters made human spines protrude further from the dendrite than in mouse (1.41±0.57μm vs 1.13±0.41μm) and with an elevated distance distally (1.34±0.51μm to 1.47±0.58μm), while in mice this value was stable (1.16±0.44μm to 1.13±0.38μm; Fig. S3F).

In mouse, spines were smaller in distal compartments than proximal (0.28±0.08 vs 0.31±0.08μm), but in human we observed the opposite effect where distal spine heads were larger than proximal ones (0.43±0.21 vs 0.4±0.17; Fig. 2G). As a result, the total spine volume fraction around the dendrite remains stable in mouse (1.87±0.24 vs 2.1±0.55%; Fig. 2H) while in human there is a trend toward higher spine volume on distal branches (4.44±1.36%) than proximal branches (3.52±0.44%). This may indicate that distal compartments amplify synaptic strength through larger spine structure to compensate for increased distance from the somatic compartment.

Human-specific 'spine cluster' structures throughout the dendritic arbor

The most notable difference between the species was the presence in humans of a previously unreported spine structure we term a "spine cluster". Unlike branched spines, spine clusters have one large head with multiple swellings that form distinct punctate structures. Individual puncta diameters are typically 0.1-0.4μm, like thin spine heads and thus perhaps constitute individual synaptic contact sites, although this could not be determined here (Fig. 2A,I and Fig. S3B). While only one of 1,380 mouse spines met the criteria, spine clusters were present across all human branches, cells, and specimens. It is conceivable that this phenomenon is a factor of aging and not species, as our human specimens came from older individuals (93 and 61yo) than our mouse specimens (12-15 weeks). However, in a tissue sample from the brain of a 37 year-old human (not included in the overall quantitative analysis) we observe spine clusters as well (Fig. S3B2). The following analyses focus on the phenomenon in human.

Spine clusters were present at an average density of 0.52±0.16/μm (Fig. 2J; included in the total of Fig. 2B) that increased distally from 0.41±0.05 to 0.62±0.17/μm (Fig. 2K; included in the total of Fig. 2C). Spine clusters typically had 4-6 puncta (4.84±1.75; Fig. 2L) and a spherical volume of 0.49±0.42μm^3 (Fig. 2M) such that the average puncta volume was 0.1μm^3—approximately that of thin spines with 0.3-0.5μm head diameters. Spine clusters had larger diameters than thin and mushroom spines (0.93±0.19 vs 0.34±0.07 and 0.58±0.07μm; Fig. S3G-H). The number of puncta, volume, and size of spine clusters were constant across compartments.

Diameter and puncta number scale linearly (Fig. 2N), suggesting that spine clusters vary in size largely through the gain or loss of discrete, stereotypically sized puncta and not through growth or shrinkage of the puncta. The increased number and trend toward increased size of spine clusters in distal compartments contributed to almost double the density of clustered puncta per dendritic length in proximal vs distal compartments (1.85±0.37 to 3.07±0.81/μm; Fig. 2O).

Climbing fiber multi-innervation may be more common in human than mouse cerebellum

While PFs are the predominant source of input onto the spines of thin dendrites, the dendritic shaft and primary dendrite are the sites of a second excitatory projection from CF axons of the inferior olive. CF innervation has been explored extensively in cat[33] and rodent models[3,34,35] and was recently updated to appreciate multi-innervation of multi-branched PCs in adult mice[4]. During development numerous CF-PC inputs undergo a competitive pruning[36–38] that may resemble adult bidirectional synaptic plasticity[39–42] and determines which CFs translocate to the dendrite. We previously hypothesized that multi-branched structure offers independent territories for CFs to evade competitive pressure. Ostensibly, being almost exclusively multi-branched may permit a higher prevalence of CF multi-innervation in humans, but we lack physiological or tract-tracing methods to test this, so only a small number of studies[43,44] have addressed adult human CFs after their first depiction by Ramón y Cajal in 1890.

To access this vital input pathway, we immunolabeled CF axonal fibers with the intermediate neurofilament protein peripherin[45]. Though extremely sparse, we identified 44 PCs with co-labeled peripherin fibers that could be classified as: “putative mono-innervation” (Fig. 3A), incompletely labeled multi-innervation we term either “absence” and “putative” multi-innervation (absence: having one fiber that is conspicuously absent from some primary dendrites, Fig. 3B; putative: having multiple truncated fibers; Fig. 3C), or “fully labeled multi-innervation” (Fig. 3D-E; see Methods). The sparsity precluded analysis of regional or foliar variation; but, taken as an average of posterior hemisphere (L6-8), the cases were classified as: putative mono-innervation (22/44), absence (11/44) or putative multi-innervation (6/44), or fully labeled multi-innervation (5/44). Thus, at least 11%, and possibly up to half of human PCs receive multiple CFs, setting the minimum likelihood to the same rate (~15%) of multi-innervation observed in mouse[4]. Variable fiber thickness and arrangement may reflect diverse CF strengths and distributions on the dendritic arbor (Fig. 3E).

This method naturally underestimates multi-innervation by distant or unlabeled CFs, but it may also be an overestimate as the labeling was not complete enough in the granule cell layer to distinguish extreme cases of “pseudo-double innervation” by converging branches of the same IO neuron axon[46]. However, the underlying PC morphology offers a modestly more concrete range. In mouse, multi-branched structure and wider dendrite separation distances elevate the rate of multi-innervation[4]. Overall, our peripherin co-labeled PCs have typical rates of multi-branched structure for human posterior hemisphere (2.3% Normative, 36.4% Split, 61.3% Poly). Mono-innervated cells, however, are less multi-branched (4.5% Normative, 41% Split, 54.5% Poly; Fig. 3F) and horizontally oriented (31.8% vertical, 68.2% horizontal; Fig. 3G) while fully labeled multi-innervated cells are more multi-branched (0% Normative, 20% Split, 80% Poly) and horizontal (20% vertical, 80% horizontal). Factors shaping the relationship between multi-branched structure and CF multi-innervation may thus be conserved across mice and humans. The demographics of intermediate classifications diverge: absence multi-innervation PCs (0% Normative, 45.5% Split, 54.5% Poly) closely align with mono-innervated PCs while putative multi-innervation PCs (0% Normative, 16.7% Split, 83.3% Poly) resemble fully labeled multi-innervated PCs (Fig. 3F). Thus, putative and fully labeled cases may in fact demarcate the same phenomenon, multi-innervation, and set the population rate to at least 25% in human.

Beyond climbing fibers, our staining reveals that segregated primary dendrite compartments can be the recipient (Fig. S4A) of narrowly branching recurrent PC axon terminals[16]. In mouse, recurrent PC axons target interneurons, PC somata[47], and superficial granule cells[48]; on rare occasion a diminutive branch will ascend into the molecular layer. We also found that primary dendrites sometimes host the axon, thereby differentiating the axon initiation site exposure to the distinct primary dendrite signals (Fig. S4B). This has not been shown in cerebellum of any species and complements our finding that PC output may be disproportionately driven by subsets of input.

Regional distributions of PC demographics in vermis are distinct from hemisphere and align with human functional boundaries

Because PC dendritic computation and input arrangement is likely shaped by morphology, we next asked whether PC morphology demographics vary across cerebellar regions in alignment with local task-specific demands. The prevalence of multi-branched PCs increases in more posterior hemisphere lobules of both species, forming an anterior-posterior gradient[4]. This may reflect that multi-branched morphology—and the input multiplexing and independent branch signaling this confers—is needed for multi-modal associative tasks performed by posterior hemisphere. If PC demographics indeed align with functional demands, we hypothesized that the cerebellar vermis, having more evolutionarily conserved somatosensory and motor functions like anterior hemisphere[49–51], would lack this gradient and demographically resemble the anterior hemisphere.

To test this, we used our previous morphological framework to categorize PCs in the vermis of human and mouse, which could be done exhaustively due to the small size of the mouse or the more sparse labeling of embalmed human tissue as compared with unembalmed tissue from previous experiments (Fig. 4A and S5A-B). Unlike the previous cell, spine, and fiber reconstructions in unembalmed tissue, the specimens used here were the same embalmed individuals as in our previous work[4]. This way, all regions can be directly compared within individual. Indeed, vermis lobules lacked a clear anterior-posterior gradient and largely resembled anterior hemisphere with an elevated rate of normative PCs and more Split than Poly PCs (Fig. 4B, bottom), though vermis PC orientations (Fig. 4B, top) better resembled posterior hemisphere (Fig. S8A-C). These regional trends were similar in the mouse (Fig. 4C-D). In human, the anterior- and posterior-most lobules (L1-2 and L9-10) diverged from the general trend by having higher rates of Poly, Normative, and vertically oriented PCs. A similar divergence was observed in the anterior-most but not posterior-most regions of the mouse. Instead, mouse L7-9 appeared distinct in having a higher rate of Poly PCs.

Local cell type clustering produces 'patchy' heterogenous processing zones within regions

Human fMRI studies demonstrate that functional boundaries do not align with the anatomical boundaries of lobules. Particularly given the size and foliation of human cerebellum, it is not clear at what spatial scale PC demographics are compiled to serve computational needs. We asked whether task-specific computational demands act on PC populations at the level of whole regions, individual folia, or smaller circuits of neighboring cells with overlapping dendrites. The distribution of PC morphologies would thus sort randomly throughout a region, be homogeneous in each folium, or exhibit 'patches' of homogeneous morphologies among neighboring PCs.

To assess demographic sorting, we first tested cell type clustering at the scale of adjacent PCs close enough to partially overlap their dendrites (Fig. 5). Each cell received a score between 0-2 to reflect how many adjacent cells matched their morphological type (Normative, Split, or Poly) and orientation (Vertical or Horizontal) along the parasagittal line of the PC layer (Fig. 5A). The rate of non-zero cluster scores was compared to a shuffled dataset (see Methods), revealing that adjacent cells with possible dendritic overlap were more likely than chance to share morphological categories (Fig. 4E). The non-random clustering rate was modestly more robust in human than mouse (17.4 vs 12.6%). Clustering was only apparent when requiring a complete match of morphological type and orientation (Fig. 5B-C), not for partial matches (Fig. S6C-D), in both vermis and hemisphere (Fig. S5F-G, S8F-G). Conceivably, clustering may produce even more precise morphological similarity among adjacent cells than surmised via broad categories. This analysis also revealed that uninterrupted clusters have on average 2.6 cells forming an inter-somatic length of 537μm in human vermis (Fig. 5B-C). In mouse, uninterrupted clusters have 3.1 cells forming a 71μm length. Compared with clusters in the vermis, clusters in the hemisphere were longer in human (2.7 cells and 838μm length; Fig. S6E-F) but identical in mouse (3 cells with 70μm length).

PC shapes are often congruent with the expansion of the molecular layer in the gyral lip or the compression in the base of the sulcus[17,52]. While this suggests that clustering may be mechanically driven by tissue foliation, we find little variation in PC demographics across foliar location (gyrus, bank, or sulcus) in human and mouse (Fig. S5C), though there were more horizontally oriented PCs in human sulcus (Fig. S5D). The same patterns were observed in hemisphere[4]. To control for foliation, we performed the same clustering analyses with shuffled

data where foliar location was held constant (see Methods). Non-random clustering was still observed (Fig. S5E), particularly in human vermis, but also in mouse and human hemisphere (Fig. S8D-E). Separating by foliar sub-area, clustering was present within bank regions—lacking bias from mechanical force—as well as the gyrus and sulcus of both vermis (Fig. S5F-G) and hemisphere (Fig. S8F-G).

It is also possible that clustering occurs among a broad population where most, but not all, cells are the same. The previous analysis could not resolve this, so we measured how well the morphology of each cell was matched by the demographics of all surrounding cells within variable distances (Fig. 5D). Non-random clustering provided an increased chance that surrounding cells had a matching morphology by ~13-14% in human and ~9-10% in mouse. Non-matching cells, inversely, had diminished likelihoods. The elevated prevalence fell below 5% within 2mm and 500μm in human and mouse, respectively, and dropped to near zero at scales roughly over 1cm and 2mm. Clustering within the core of a measured area could artificially inflate the rate of drop-off, so we next sampled only cells surrounding variably sized core regions (Fig. 5E). This revealed that clustering was largely restricted to a 2mm and 400μm range in human and mouse, respectively. The scale of non-random clustering in the hemisphere extended to 3mm in human and held at 400μm in mouse (Fig. S7).

Inter-hemisphere PC demographic similarity covaries with functional symmetry

As some lobules have higher functional asymmetry across hemispheres in human[49,53–56], we hypothesized that inter-hemisphere PC demography might reflect these patterns if it is related to function. Functionally symmetric regions (e.g. L5-L6) may then exhibit more similar PC demographics than highly asymmetric regions (eg. Crus I-II). To test this, we compared PC demographics in lobules 5-Crus II of the opposing hemisphere of specimens from which we previously examined one hemisphere[4] (Fig. 6A-B and S8A-B). We now show that the previously described anterior-posterior gradient is a *bilateral* phenomenon, as Poly PCs were universally more prevalent in Crus I/II than L5-6 (Fig. 6C). The inter-hemisphere rate of PC sub-types varied more in Crus I/II than L5 and especially L6 (Fig. 6D). Averaging the difference across morphologies (Fig. 6E), the mean inter-hemisphere demographic variation of each lobule confirmed that L5 and 6 exhibited less variation (2.9±1.63 and 2.17±1.35%) than Crus I and II (5.03±2.88 and 4.21±2.26%). Due to high inter-individual variation, we normalized the rate of variation in L5, Crus I, and Crus II to that of L6 within individuals. This revealed that all lobules had more variation.

Discussion

Our histological interrogation of Purkinje cells in post-mortem human and mouse tissue defines human PC morphology and input arrangement as both *quantitatively* and *qualitatively* distinct from the rodent model. Recent work using developmental and spatial transcriptomics in human tissue has revealed that PCs are genetically diverse[57–60] and present with several putatively human-specific sub-types[61]. Variable genetic profiles may factor into the diversification of PC morphology within species and may also underlie the human-specific features observed here. In clarifying how the species diverge, this work highlights the importance of further anatomical study in human but also strengthens the interpretability of disease studies that must by necessity be pursued in animal and *in silico* models[20]. Dendrite morphology may factor into cerebellar disease etiology. In mouse, PC morphology and CF signaling is altered in disease models such as spinocerebellar ataxia[62,63] and syndromic autism[64–66]. On the only occasions that human PC dendritic morphology has been measured with respect to cerebellar disease, it was disrupted in Essential Tremor[19,22] and Friedrichs Ataxia[67] and dendritic abnormalities were recently reported in Spinocerebellar Ataxias and other neurodegenerative movement disorders[68].

Are human PCs an allometrically scaled mouse PC?

Human PCs are substantially larger than those of the mouse. But are they *just* allometrically scaled mouse PCs? The answer is likely no. Only some features appear to be either invariant or proportionally scaled with molecular layer thickness. We observed similar fractal branching patterns and relative average distances of peak branch number and dendritic length from the soma, suggesting a possible shared dependence on cell

autonomous factors governing the branching pattern. The diameter of thin caliber dendrites is identical, indicating a shared constraint on dendritic thickness perhaps by limits of physiological conduction.

The dimensions of the cerebellar cortex are a plausible allometric constraint on cellular growth. Yet, human PCs expand their size well beyond the relative difference in molecular layer thickness— reflected by PC height—by multiplying and extending their primary dendrites outward in the parasagittal axis to articulate an expanded horizontal profile. The horizontal eccentricities of non-primary dendrites further drive the extended width of human PCs and permit spiny branches to double back, overlap in distinct mediolateral planes, and possibly resurvey the PF axons projecting through the arbor. The latter feature could expand combinatorial coding by human PC dendritic branches without requiring increased granule cell or PF densities. Human PCs also exhibit more variable morphological features across locations in the arbor, such as having a rapid rise and decline in branch location, total length, and branching order relative to the position of the soma. The complexity of this distribution is distinct from mouse PCs where these properties are maintained homogeneously through most of their structure. More variable branch lengths may also diversify independent signaling capacity across the arbor. While this cannot currently be tested directly, the confluence of invariant, allometric, and non-allometric morphological features may indicate that human PC physiology diverges from the rodent not only as a matter of scale[20] but as a matter of kind.

Enhanced and human-specific features of input amplification and association by dendritic spines

Qualitative, unlike *quantitative*, species differences are uncommon. We observed human-specific spine clusters that—to the best of our knowledge—have not been described before. These clusters certainly deserve further histological and functional characterization that was beyond the scope of this study. Spine clusters may be potentially fertile ground to explore new modes of synaptic and dendritic signaling. Some features—larger size and possibly more postsynaptic densities—represent quantitative expansion, but others may represent novel physiological phenomena. First, unlike branched or calyx spines[31,32], several synaptic contacts would be exposed to membrane potentials and cytosolic plasticity factors in common. Second, while not quantified here, clustered inputs may operate in variable isolation from the dendrite and other local synapses as the neck diameter varies widely from the conserved value of 0.1-0.3μm[29,69] to 0.5-0.7μm (Fig. 2A,I). The latter would have low electrical resistance, more contiguity with the dendritic shaft, and therefore behave like a small dendritic sub-branchlet. Indeed, spine clusters protrude ~1.5-3μm, echoing the 2-4μm length of the smallest terminal dendritic branchlets in the mouse. These two features may combine to produce both an associative structure, like proposed for branched spines[32], and a new form of amplifying structure providing the substrate to initiate dendritic calcium spikes[11,70,71].

In addition to spine clusters, human PCs are more spine dense and thus may receive disproportionately more inputs than rodent PCs. The spine density we observe in mouse differs from studies reporting 1-2/μm—or the frequently cited work in rat reporting, by extrapolation, ~17/μm[72]—but are in perfect agreement with recent confocal[73] and EM reconstructions[28,32,74–77]. Our data reveal elevated spine density in distal compartments, which comports with the knowledge that distal compartments receive denser PF innervation[17]. We also show that branched spine density increases distally, possibly supporting their proposed role in associative PF plasticity, a critical feature of the perceptron model[32,78]. Larger spine heads in human may strengthen post-synaptic signaling so a higher percentage of inputs can influence PC output than in mouse. Alternatively, this amplification may simply compensate for human PC size, an idea supported by the fact that in human, unlike mouse, the spines are larger in distal compartments. Possibly reflecting shared factors of increased computational complexity and compensation for size or compartmentalization[79], pyramidal cells have similarly greater spine density (pyramidal: 1.3x vs Purkinje: 1.41x) and size (1.27x vs 1.41x)[80,81].

Human Purkinje dendrite size and input numerosity

The previously reported average human PC dendritic length was 10-20,000μm, varying with methodology (Golgi impregnation[19,23] vs post-fix dye electroporation[20]). Our current knowledge, then, would conclude that human PCs are the same size as pyramidal cells (L2/3 are ~14,500μm, <22,000μm[82]; thick tufted L5/6 are ~1-2000μm longer[82]; hippocampal CA1 are ~18,600μm, <27,000μm[83]). While one might naturally expect the 2D radiations of PCs to make them larger in human than 1D radiating pyramidal cells, the previous data would

suggest instead that there is a ceiling for maximal neuronal size and that, in human, both cell types met that limit before diverging. On the contrary, we demonstrate for the first time that PCs are substantially bigger than pyramidal cells and boast the largest dendritic arbor of any recorded neuron in the human brain. Intriguingly, our findings also indicate that pyramidal and Purkinje cells scale differently in mouse (~5,500 vs ~6,000μm) than human (~15,000 vs ~65,000μm).

With higher spine density and longer spiny dendrites, we can extrapolate that human PCs likely host half a million spines compared to ~30,000 in mouse. Branched spines (~7% of spines in both species) can host synapses with two PF axons while spine clusters (~10% in human) may host over four. As such, the human may receive ~750,000 synaptic inputs on spines. It is not only staggering to consider a single neuron receiving ~1 million inputs, but it highlights that the species' dendritic length ratio (11:1) belies an input ratio around 30:1.

Human PCs multiplex CFs and other inputs

We previously found more multi-innervated PCs in posterior lobules of mouse[4], likely due to the heightened prevalence of multi-branched PCs. This was recently replicated, albeit tangentially[84]. We predicted that multi-branched structure permits CF multi-innervation by providing segregated synaptic territories where multiple CFs could avoid the competitive pruning that would have prevented their translocation from soma to dendrite. This prediction was also supported by our finding that surplus CFs had greater synaptic strength in older animals[4], possibly reflecting a delayed or elongated maturation process following distinct developmental trajectories of presynaptic plasticity at weak versus strong CF inputs before P21[85].

Human PC dendrites commonly ramify in more horizontal eccentricities than in mouse. This produces a distinct multi-branched motif with primary dendrites ramifying outward and giving rise to numerous (around 7-8) sub-compartments, each ~5-10,000μm in length — roughly an entire rodent cell. Dendrite width complements multi-branched structure to further enable CF multi-innervation in mouse[4]. Here, co-immunolabeling of calbindin and peripherin[45] provides the first demonstration of CF multi-innervation in adult human. It also extends to humans the hypothesis that multi-branched structure supports CF competition avoidance. Finally, our co-labeling supports a likely higher prevalence of multi-innervation than in mouse.

Cerebellar cortical geometry allows us to speculate that a horizontally aligned dendritic arbor—often almost a millimeter wide (Fig 1A,G)—would allow human PCs to receive input from highly segregated excitatory PFs from distant granule cells. If conserved, spatial-functional PF clustering reported in mouse[86] would make their functional similarity diminish with distance. Thus, the disproportionate width of human PCs may sample more distinct PF representations. Similarly, this dendritic width may engender more compartment-specific inhibition by molecular layer interneurons[87] and oversampling of modulatory influence by vertically ascending cholinergic beaded fibers[88] and Bergmann glia[89]. Taken together, human PCs likely perform highly complex input multiplexing and dendritic computations that are unlike what is commonly reported in mouse. This would, in turn, distinguish human PC dendritic plasticity and output information content as distinct from mouse PCs.

Studies of PC computation have largely considered the dendritic arbor a continuous functional compartment due to the equally unusual singularity and numerousness of CF and PF input, respectively. More recently, experimental and modeling studies demonstrate that Purkinje dendrite compartments exhibit heterogeneous ion channel density and plasticity[9,10], localized calcium signals[11,90], PF input clustering[86], and variable calcium signaling due to branch shape in a homogeneous channel model[7,12,13]. Combined with the finding that some PC dendrites are innervated by multiple CFs that confer branch-specific signaling[4], the potential for dendritic input multiplexing is becoming more widely appreciated[12].

We previously suggested that CF multi-innervation may be an adaptation to maintain receptive field matching in multi-branched PCs with more disparate PF representations across segregated dendritic compartments[4]. This would preserve perceptron function among mouse PCs with expanded dendritic arbors. Our findings extend this concept to human PCs where there is likely a greater demand to match distinct receptive fields. As a possible consequence, human PC output may convey more features of sensory, internal, or cognitive state. Individual CFs convey a variety of signals[91–93]. PF-dependent simple spike modulation reflects unidimensional movement kinematics in oculomotor L6-7[94], but can represent multiple proprioceptive features in anterior vermis during passive vestibular stimulation[95] and reinforcement learning error and learning state during a visuomotor association task among Crus1-2 PCs[96] where multi-branched structure is more common.

Thus, multi-branched PC computation may resemble mixed selectivity encoding by pyramidal cells involved in complex decision-making[97]. Importantly, expansion of input numerosity or strength does not necessarily improve computational capacity. Excess CF innervation is linked to cellular and behavioral sensory over-responsiveness in mouse autism models[64,65]. Human essential tremor is characterized in part by excess CF innervation from ectopic lateral crossings[44] and translocation to thin dendrites[98].

Human cerebellum may harness regional PC demographics and sub-regional clustering to generate task-specific computation

We previously described a parasagittal gradient of PC morphological demographics in human and mouse mid-hemisphere[4]. Here, we control for a possible role of parasagittal developmental gradients[99] both through comparison with the vermis—with a distinct demographic gradient despite shared parasagittal development—and by showing that inter-hemisphere demographic similarity covaries with functional symmetry[49,50,53–55,100]. In mouse, posterior hemisphere processes multisensory information from mossy fibers[101–103] and CFs[64,65,91,92,104–107] and receive stronger somatosensory feedback from neocortex than the vermis[108]. In human, lateral and posterior regions are more responsive to cognitive, affective, and socio-linguistic information[53,109–111] and, intriguingly, exhibit stronger hyper-allometric expansion than the cerebrum and the rest of cerebellum in primates[112].

We propose that the relative proportions of multidendritic structure and horizontal orientation act as complementary toggles to generate four classes of morphological demography. Surprisingly, the regional borders of each class align well with four functional classes from a new consensus atlas of human cerebellum[49] (Fig. S9). Furthermore, regions with more complex morphology (increased multi-branched and horizontal orientation) roughly match regions processing information that is more cognitive (co-active with non-primary sensory neocortical regions) and associative (requiring integration and association of multi-modal inputs) in nature (Fig. S9).

Sub-regional clustering is more prevalent in human and only partly reflective of developmental tissue foliation. The spatial scale of clustering and the comparative scale ratio (~5-7x longer in human; enhanced clustering in core regions of 2mm vs 400μm) are congruent with the absolute and relative widths of the dendritic arbor. Both properties support the idea that neighboring cells' primary dendrites may reciprocally influence each other during development. Notably, the clustering scale ratio exceeds the comparative PC height ratio (a proxy for allometric constraint). This comports with observations that segregated branches of multidendritic mouse PCs often stagger in interdigitated dendrite arbors with lower medio-lateral overlap[6]. This suggests that cerebellar cortical region, especially in human, may employ "patches" of homogeneous PC morphologies to create niches for heterogeneous computations. Non-random spatial clustering of neuronal cells by morphological sub-type has not previously been described in other brain areas, potentially making this a cerebellum-specific means to boost functional diversity.

Acknowledgements

For valuable advice and technical support, we thank Hansel lab members T.-F. Lin, A. Silbaugh, D. Huang, and A. Ferrell. We thank R. A. Eatock, W. Wei, M. Sheffield, and P. Mason (UChicago Neurobiology) for insightful discussions and crucial feedback on the manuscript. Human tissue was made available by the Anatomical Gift Association of Illinois and by the New York Brain Bank with the assistance of Dr. Phyllis Faust (Columbia University). This work was supported by: National Institutes of Health (NINDS) grant R21NS124217 (CH) and F31NS129256 (SEB).

Author Contributions

Conceptualization, S.E.B. and C.H.; Formal Analysis, S.E.B.; Investigation, S.E.B.; Data Curation, S.E.B.; Writing — Original Draft, S.E.B.; Writing — Review and Editing, S.E.B. and C.H.; Visualization, S.E.B.; Supervision, C.H.; Funding Acquisition, S.E.B. and C.H.

Declaration of Interests

The authors declare no competing interests.

References

1. Albus, J. S. A theory of cerebellar function. *Mathematical Biosciences* **10**, 25–61 (1971).

2. Marr, D. A theory of cerebellar cortex. *The Journal of Physiology* **202**, 437–470 (1969).

3. Ito, M. & Kano, M. Long-lasting depression of parallel fiber-Purkinje cell transmission induced by conjunctive stimulation of parallel fibers and climbing fibers in the cerebellar cortex. *Neuroscience Letters* **33**, 253–258 (1982).

4. Busch, S. E. & Hansel, C. Climbing fiber multi-innervation of mouse Purkinje dendrites with arborization common to human. *Science* **381**, 420–427 (2023).

5. Kaneko, M. *et al.* Remodeling of monoplanar purkinje cell dendrites during cerebellar circuit formation. *PLoS ONE* **6**, 1–13 (2011).

6. Nedelescu, H., Abdelhack, M. & Pritchard, A. T. Regional differences in Purkinje cell morphology in the cerebellar vermis of male mice. *Journal of Neuroscience Research* **96**, 1476–1489 (2018).

7. Zang, Y., Dieudonné, S. & De Schutter, E. Voltage- and Branch-Specific Climbing Fiber Responses in Purkinje Cells. *Cell reports* **24**, 1536–1549 (2018).

8. Midtgaard, J. Spatial synaptic integration in Purkinje cell dendrites. *The Journal of Physiology* **89**, 23–32 (1995).

9. Ohtsuki, G. Modification of Synaptic-Input Clustering by Intrinsic Excitability Plasticity on Cerebellar Purkinje Cell Dendrites. *J. Neurosci.* **40**, 267–282 (2020).

10. Ohtsuki, G., Piochon, C., Adelman, J. P. & Hansel, C. SK2 channel modulation contributes to compartment-specific dendritic plasticity in cerebellar Purkinje cells. *Neuron* **75**, 108–120 (2012).

11. Roome, C. J. & Kuhn, B. Simultaneous dendritic voltage and calcium imaging and somatic recording from Purkinje neurons in awake mice. *Nature Communications* **9**, 1–14 (2018).

12. Zang, Y. & De Schutter, E. The Cellular Electrophysiological Properties Underlying Multiplexed Coding in Purkinje Cells. *J. Neurosci.* **41**, 1850–1863 (2021).

13. Cirtala, G. & De Schutter, E. Branch-specific clustered parallel fiber input controls dendritic computation in Purkinje cells. *iScience* 110756 (2024) doi:10.1016/j.isci.2024.110756.

14. Lin, T.-F., Busch, S. E. & Hansel, C. Intrinsic and synaptic determinants of receptive field plasticity in Purkinje cells of the mouse cerebellum. *Nat Commun* **15**, 4645 (2024).

15. Golgi, C. *Sulla fina anatomia del cervelletto umano*. vol. 2 (Archivio Italiano per le Malattie Nervose, 1874).

16. Ramón y Cajal, S. *Histologie du système nerveux de l'homme & des vertébrés*. (Paris□: Maloine, 1909).

17. Eccles, J. C., Ito, M. & Szentágothai, J. *The Cerebellum as a Neuronal Machine*. (Springer, Berlin, Heidelberg, 1967). doi:10.1007/978-3-662-13147-3.

18. Kato, T., Hirano, A. & Llena, J. F. A Golgi study of the human Purkinje cell soma and dendrites. *Acta Neuropathol* **68**, 145–148 (1985).

19. Louis, E. D. *et al.* Reduced Purkinje cell dendritic arborization and loss of dendritic spines in essential tremor. *Brain* **137**, 3142–3148 (2014).

20. Masoli, S. *et al.* Human Purkinje cells outperform mouse Purkinje cells in dendritic complexity and computational capacity. *Commun Biol* **7**, 1–18 (2024).

21. Mavroudis, I. A. *et al*. Purkinje cells pathology in schizophrenia. A morphometric approach. *Rom J Morphol Embryol* **58**, 419–424 (2017).

22. Mavroudis, I. A. *et al*. Morphological and morphometric changes in the Purkinje cells of patients with essential tremor. *Experimental and Therapeutic Medicine* **23**, 1–8 (2022).

23. Ruela, C., Matos-Lima, L., Sobrinho-Simoes, M. A. & Paula-Barbosa, M. M. Comparative morphometric study of cerebellar neurons. *Acta anat* **106**, 270–275 (1980).

24. Gao, Y. *et al.* -III Spectrin Is Critical for Development of Purkinje Cell Dendritic Tree and Spine Morphogenesis. *Journal of Neuroscience* **31**, 16581–16590 (2011).

25. Takeo, Y. H. *et al.* GluD2- and Cbln1-mediated competitive interactions shape the dendritic arbors of cerebellar Purkinje cells. *Neuron* **109**, 629-644.e8 (2021).

26. Joo, W., Hippenmeyer, S. & Luo, L. Dendrite morphogenesis depends on relative levels of NT-3/TrkC signaling. *Science* **346**, 626–629 (2014).

27. Kano, M., Watanabe, T., Uesaka, N. & Watanabe, M. Multiple Phases of Climbing Fiber Synapse Elimination in the Developing Cerebellum. *Cerebellum* **17**, 722–734 (2018).

28. Nguyen, T. M. *et al.* Structured cerebellar connectivity supports resilient pattern separation. *Nature* **613**, 543–549 (2023).

29. Harris, K. M. & Stevens, J. K. Dendritic spines of rat cerebellar Purkinje cells: serial electron microscopy with reference to their biophysical characteristics. *J. Neurosci*. **8**, 4455–4469 (1988).

30. Lee, K. J., Kim, H., Kim, T. S., Park, S.-H. & Rhyu, I. J. Morphological analysis of spine shapes of Purkinje cell dendrites in the rat cerebellum using high-voltage electron microscopy. *Neuroscience Letters* **359**, 21–24 (2004).

31. Lee, K. J., Kim, H. & Rhyu, I. J. The roles of dendritic spine shapes in Purkinje cells. *Cerebellum* **4**, 97–104 (2005).

32. Loschky, S. S. *et al.* Ultrastructural effects of sleep and wake on the parallel fiber synapses of the cerebellum. *eLife* **11**, e84199 (2022).

33. Eccles, J. C., Llinás, R. & Sasaki, K. The excitatory synaptic action of climbing fibres on the Purkinje cells of the cerebellum. *The Journal of Physiology* **182**, 268–296 (1966).

34. Maekawa, K. & Simpson, J. I. Climbing fiber activation of Purkinje cells in the flocculus by impulses transferred through the visual pathway. *Brain Research* **39**, 245–251 (1972).

35. Simpson, J. I., Wylie, D. & De Zeeuw, C. On climbing fiber signals and their consequence(s). *Behavioral and Brain Sciences* **1996**, 384–398 (1996).

36. Hashimoto, K., Ichikawa, R., Kitamura, K., Watanabe, M. & Kano, M. Translocation of a "Winner" Climbing Fiber to the Purkinje Cell Dendrite and Subsequent Elimination of "Losers" from the Soma in Developing Cerebellum. *Neuron* **63**, 106–118 (2009).

37. Hashimoto, K. & Kano, M. Functional differentiation of multiple climbing fiber inputs during synapse elimination in the developing cerebellum. *Neuron* **38**, 785–796 (2003).

38. Wilson, A. M. *et al.* Developmental Rewiring between Cerebellar Climbing Fibers and Purkinje Cells Begins with Positive Feedback Synapse Addition. *Cell Reports* **29**, 2849-2861.e6 (2019).

39. Bosman, L. W. J., Takechi, H., Hartmann, J., Eilers, J. & Konnerth, A. Homosynaptic Long-Term Synaptic Potentiation of the "Winner" Climbing Fiber Synapse in Developing Purkinje Cells. *J. Neurosci.* **28**, 798–807 (2008).

40. Hansel, C. & Linden, D. J. Long-term depression of the cerebellar climbing fiber-Purkinje neuron synapse. *Neuron* **26**, 473–482 (2000).

41. Ohtsuki, G. & Hirano, T. Bidirectional plasticity at developing climbing fiber–Purkinje neuron synapses. *European Journal of Neuroscience* **28**, 2393–2400 (2008).

42. Piochon, C., Kano, M. & Hansel, C. LTD-like molecular pathways in developmental synaptic pruning. *Nature Neuroscience* **19**, 1299–1310 (2016).

43. Lin, C.-Y. *et al.* Abnormal climbing fibre-Purkinje cell synaptic connections in the essential tremor cerebellum. *Brain* **137**, 3149–3159 (2014).

44. Wu, Y.-C. *et al.* Increased Climbing Fiber Lateral Crossings on Purkinje Cell Dendrites in the Cerebellar Hemisphere in Essential Tremor. *Movement Disorders* **36**, 1440–1445 (2021).

45. Errante, L. *et al.* The intermediate filament protein peripherin is a marker for cerebellar climbing fibres. *J Neurocytol* **27**, 69–84 (1998).

46. Sugihara, I., Wu, H. S. & Shinoda, Y. Morphology of single olivocerebellar axons labeled with biotinylated dextran amine in the rat. *Journal of Comparative Neurology* **414**, 131–148 (1999).

47. Witter, L., Rudolph, S., Pressler, R. T., Lahlaf, S. I. & Regehr, W. G. Purkinje Cell Collaterals Enable Output Signals from the Cerebellar Cortex to Feed Back to Purkinje Cells and Interneurons. *Neuron* **91**, 312–319 (2016).

48. Guo, C. *et al.* Purkinje Cells Directly Inhibit Granule Cells in Specialized Regions of the Cerebellar Cortex. *Neuron* **91**, 1330–1341 (2016).

49. Nettekoven, C. *et al*. A hierarchical atlas of the human cerebellum for functional precision mapping. 2023.09.14.557689 Preprint at https://doi.org/10.1101/2023.09.14.557689 (2024).

50. Buckner, R. L., Krienen, F. M., Castellanos, A., Diaz, J. C. & Yeo, B. T. T. The organization of the human cerebellum estimated by intrinsic functional connectivity. *Journal of Neurophysiology* **106**, 2322–2345 (2011).

51. Saadon-Grosman, N., Angeli, P. A., DiNicola, L. M. & Buckner, R. L. A third somatomotor representation in the human cerebellum. *Journal of Neurophysiology* **128**, 1051–1073 (2022).

52. Friede, R. Quantitative displacement of the layers within the convolutions of the cerebellar cortex and its biologic importance. *Acta anatomica* **25**, 65–72 (1955).

53. Stoodley, C. J. & Schmahmann, J. D. Functional topography in the human cerebellum: A meta-analysis of neuroimaging studies. *NeuroImage* **44**, 489–501 (2009).

54. Wang, D., Buckner, R. L. & Liu, H. Cerebellar asymmetry and its relation to cerebral asymmetry estimated by intrinsic functional connectivity. *Journal of Neurophysiology* **109**, 46–57 (2013).

55. Wang, D., Buckner, R. L. & Liu, H. Functional Specialization in the Human Brain Estimated By Intrinsic Hemispheric Interaction. *J. Neurosci*. **34**, 12341–12352 (2014).

56. O'Reilly, J. X., Beckmann, C. F., Tomassini, V., Ramnani, N. & Johansen-Berg, H. Distinct and Overlapping Functional Zones in the Cerebellum Defined by Resting State Functional Connectivity. *Cerebral Cortex* **20**, 953–965 (2010).

57. Sepp, M. *et al.* Cellular development and evolution of the mammalian cerebellum. *Nature* **625**, 788–796 (2024).

58. Zhong, S. *et al.* Single-cell epigenomics and spatiotemporal transcriptomics reveal human cerebellar development. *Nat Commun* **14**, 7613 (2023).

59. Aldinger, K. A. *et al.* Spatial and cell type transcriptional landscape of human cerebellar development. *Nat Neurosci* **24**, 1163–1175 (2021).

60. Kozareva, V. *et al*. A transcriptomic atlas of mouse cerebellar cortex comprehensively defines cell types. *Nature* **598**, 214–219 (2021).

61. Buchholz, D. E. *et al.* Novel genetic features of human and mouse Purkinje cell differentiation defined by comparative transcriptomics. *Proceedings of the National Academy of Sciences* **117**, 15085–15095 (2020).

62. Du, X. *et al.* Second Cistron in CACNA1A Gene Encodes a Transcription Factor Mediating Cerebellar Development and SCA6. *Cell* **154**, 118–133 (2013).

63. Du, X. *et al*. α1ACT Is Essential for Survival and Early Cerebellar Programming in a Critical Neonatal Window. *Neuron* **102**, 770-785.e7 (2019).

64. Simmons, D. H. *et al.* Sensory Over-responsivity and Aberrant Plasticity in Cerebellar Cortex in a Mouse Model of Syndromic Autism. *Biological Psychiatry Global Open Science* **2**, 450–459 (2022).

65. Busch, S. E. *et al*. Overexpression of the autism candidate gene Cyfip1 pathologically enhances olivo-cerebellar signaling in mice. *Frontiers in Cellular Neuroscience* **17**, (2023).

66. Piochon, C. *et al.* Cerebellar plasticity and motor learning deficits in a copy-number variation mouse model of autism. *Nature Communications* **5**, 1–12 (2014).

67. Kemp, K. C. *et al*. Purkinje cell injury, structural plasticity and fusion in patients with Friedreich's ataxia. *Acta Neuropathologica Communications* **4**, 53 (2016).

68. Louis, E. D. *et al.* Histopathology of the cerebellar cortex in essential tremor and other neurodegenerative motor disorders: comparative analysis of 320 brains. *Acta Neuropathol* **145**, 265–283 (2023).

69. Ofer, N., Berger, D. R., Kasthuri, N., Lichtman, J. W. & Yuste, R. Ultrastructural analysis of dendritic spine necks reveals a continuum of spine morphologies. *Developmental Neurobiology* **81**, 746–757 (2021).

70. Eilers, J., Augustine, G. J. & Konnerth, A. Subthreshold synaptic Ca2+ signalling in fine dendrites and spines of cerebellar Purkinje neurons. *Nature* **373**, 155–158 (1995).

71. Hartell, N. A. Strong Activation of Parallel Fibers Produces Localized Calcium Transients and a Form of LTD That Spreads to Distant Synapses. *Neuron* **16**, 601–610 (1996).

72. Napper, R. M. A. & Harvey, R. J. Number of parallel fiber synapses on an individual Purkinje cell in the cerebellum of the rat. *Journal of Comparative Neurology* **274**, 168–177 (1988).

73. O'Brien, J. & Unwin, N. Organization of spines on the dendrites of Purkinje cells. *Proceedings of the National Academy of Sciences* **103**, 1575–1580 (2006).

74. Hillman, D. E. & Chen, S. Reciprocal relationship between size of postsynaptic densities and their number: Constancy in contact area. *Brain Research* **295**, 325–343 (1984).

75. Ichikawa, R. *et al*. Territories of heterologous inputs onto Purkinje cell dendrites are segregated by mGluR1-dependent parallel fiber synapse elimination. *Proceedings of the National Academy of Sciences* **113**, 2282–2287 (2016).

76. Lu, H., Esquivel, A. V. & Bower, J. M. 3D electron microscopic reconstruction of segments of rat cerebellar purkinje cell dendrites receiving ascending and parallel fiber granule cell synaptic inputs. *Journal of Comparative Neurology* **514**, 583–594 (2009).

77. Špaček, J. & Hartmann, M. Three-Dimensional analysis of dendritic spines. *Anat Embryol* **167**, 289–310 (1983).

78. Brunel, N., Hakim, V., Isope, P., Nadal, J.-P. & Barbour, B. Optimal Information Storage and the Distribution of Synaptic Weights: Perceptron versus Purkinje Cell. *Neuron* **43**, 745–757 (2004).

79. Beaulieu-Laroche, L. *et al.* Enhanced Dendritic Compartmentalization in Human Cortical Neurons. *Cell* **175**, 643-651.e14 (2018).

80. Benavides-Piccione, R., Ballesteros-Yáñez, I., DeFelipe, J. & Yuste, R. Cortical area and species differences in dendritic spine morphology. *J Neurocytol* **31**, 337–346 (2002).

81. Benavides-Piccione, R., Fernaud-Espinosa, I., Robles, V., Yuste, R. & DeFelipe, J. Age-Based Comparison of Human Dendritic Spine Structure Using Complete Three-Dimensional Reconstructions. *Cerebral Cortex* **23**, 1798–1810 (2013).

82. Mohan, H. *et al.* Dendritic and Axonal Architecture of Individual Pyramidal Neurons across Layers of Adult Human Neocortex. *Cereb Cortex* **25**, 4839–4853 (2015).

83. Mertens, E. J. *et al.* Morpho-electric diversity of human hippocampal CA1 pyramidal neurons. *Cell Reports* **43**, (2024).

84. Nakayama, H. *et al.* Direct and indirect pathways for heterosynaptic interaction underlying developmental synapse elimination in the mouse cerebellum. *Commun Biol* **7**, 1–13 (2024).

85. Pätz, C., Brachtendorf, S. & Eilers, J. Developmental Easing of Short-Term Depression in “Winner” Climbing Fibers. *Frontiers in Cellular Neuroscience* **13**, 1–9 (2019).

86. Wilms, C. D. & Häusser, M. Reading out a spatiotemporal population code by imaging neighbouring parallel fibre axons in vivo. *Nature Communications* **6**, (2015).

87. Lackey, E. P. *et al.* Specialized connectivity of molecular layer interneuron subtypes leads to disinhibition and synchronous inhibition of cerebellar Purkinje cells. *Neuron* **112**, 2333–2348 (2024).

88. Barmack, N. H., Baughman, R. W. & Eckenstein, F. P. Cholinergic innervation of the cerebellum of rat, rabbit, cat, and monkey as revealed by choline acetyltransferase activity and immunohistochemistry. *Journal of Comparative Neurology* **317**, 233–249 (1992).

89. De Zeeuw, C. I. & Hoogland, T. M. Reappraisal of Bergmann glial cells as modulators of cerebellar circuit function. *Front. Cell. Neurosci.* **9**, (2015).

90. Kitamura, K. & Häusser, M. Dendritic Calcium Signaling Triggered by Spontaneous and Sensory-Evoked Climbing Fiber Input to Cerebellar Purkinje Cells In Vivo. *Journal of Neuroscience* **31**, 10847–10858 (2011).

91. Gaffield, M. A., Bonnan, A. & Christie, J. M. Conversion of Graded Presynaptic Climbing Fiber Activity into Graded Postsynaptic Ca2+ Signals by Purkinje Cell Dendrites. *Neuron* **102**, 1–8 (2019).

92. Ju, C. *et al.* Neurons of the inferior olive respond to broad classes of sensory input while subject to homeostatic control. *Journal of Physiology* **597**, 2483–2514 (2019).

93. Kostadinov, D., Beau, M., Pozo, M. B. & Häusser, M. Predictive and reactive reward signals conveyed by climbing fiber inputs to cerebellar Purkinje cells. *Nature Neuroscience* **22**, 950–962 (2019).

94. Pi, J. S. *et al*. The olivary input to the cerebellum dissociates sensory events from movement plans. *Proceedings of the National Academy of Sciences* **121**, e2318849121 (2024).

95. Zobeiri, O. A. & Cullen, K. E. Distinct representations of body and head motion are dynamically encoded by Purkinje cell populations in the macaque cerebellum. *eLife* **11**, e75018 (2022).

96. Sendhilnathan, N., Goldberg, M. E. & Ipata, A. E. Mixed Selectivity in the Cerebellar Purkinje-Cell Response during Visuomotor Association Learning. *J. Neurosci.* **42**, 3847–3855 (2022).

97. Tye, K. M. *et al.* Mixed selectivity: Cellular computations for complexity. *Neuron* **112**, 2289–2303 (2024).

98. Pan, M.-K. *et al.* Cerebellar oscillations driven by synaptic pruning deficits of cerebellar climbing fibers contribute to tremor pathophysiology. *Science Translational Medicine* **12**, eaay1769 (2020).

99. Beekhof, G. C. *et al*. Differential spatiotemporal development of Purkinje cell populations and cerebellum-dependent sensorimotor behaviors. *eLife* https://elifesciences.org/articles/63668/figures (2021) doi:10.7554/eLife.63668.

100. Krienen, F. M. & Buckner, R. L. Segregated Fronto-Cerebellar Circuits Revealed by Intrinsic Functional Connectivity. *Cerebral Cortex* **19**, 2485–2497 (2009).

101. Huang, C.-C. *et al.* Convergence of pontine and proprioceptive streams onto multimodal cerebellar granule cells. *eLife* **2**, e00400 (2013).

102. Ishikawa, T., Shimuta, M. & Häusser, M. Multimodal sensory integration in single cerebellar granule cells in vivo. *eLife* **4**, e12916 (2015).

103. Shimuta, M., Sugihara, I. & Ishikawa, T. Multiple signals evoked by unisensory stimulation converge onto cerebellar granule and Purkinje cells in mice. *Communications Biology* **3**, 1–12 (2020).

104. Bosman, L. W. J. *et al.* Encoding of whisker input by cerebellar Purkinje cells. *The Journal of Physiology* **588**, 3757–3783 (2010).

105. Ohmae, S. & Medina, J. F. Climbing fibers encode a temporal-difference prediction error during cerebellar learning in mice. *Nature Neuroscience* **18**, 1798–1803 (2015).

106. Rondi-Reig, L., Paradis, A.-L., Lefort, J. M., Babayan, B. M. & Tobin, C. How the cerebellum may monitor sensory information for spatial representation. *Front. Syst. Neurosci.* **8**, (2014).

107. De Zeeuw, C. I. *et al.* Microcircuitry and function of the inferior olive. *Trends in Neurosciences* **21**, 391–400 (1998).

108. Pisano, T. J. *et al.* Homologous organization of cerebellar pathways to sensory, motor, and associative forebrain. *Cell Reports* **36**, (2021).

109. LeBel, A. & D'Mello, A. M. A seat at the (language) table: incorporating the cerebellum into frameworks for language processing. *Current Opinion in Behavioral Sciences* **53**, 101310 (2023).

110. Van Overwalle, F., D'aes, T. & Mariën, P. Social cognition and the cerebellum: A meta-analytic connectivity analysis. *Human Brain Mapping* **36**, 5137–5154 (2015).

111. LeBel, A., Jain, S. & Huth, A. G. Voxelwise Encoding Models Show That Cerebellar Language Representations Are Highly Conceptual. *J. Neurosci.* **41**, 10341–10355 (2021).

112. Magielse, N., Heuer, K., Toro, R., Schutter, D. J. L. G. & Valk, S. L. A Comparative Perspective on the Cerebello-Cerebral System and Its Link to Cognition. *Cerebellum* **22**, 1293–1307 (2023).

Methods

Subjects Human cerebellar tissue was collected from three unembalmed and three embalmed donor bodies provided by the Anatomical Gift Association of Illinois (AGAI) and the New York Brain Bank (NYBB). Unembalmed individuals were 93 (F), 61 (M), and 37 (M) and died of causes unrelated to cerebellar morphology (e.g. chronic obstructive pulmonary disease, bile duct cancer, and hypertrophic cardiomyopathy, respectively). The first two cadavers were stored for 6 and 7 days before fixation. Embalmed individuals were 92 (F), 95 (F), and 86 (M) years old and died of causes unrelated to cerebellar morphology (e.g. 'failure to thrive', likely 'failure to thrive', and colon cancer, respectively). Cadavers were stored for 2, 6, and 2 months, respectively. During life, all study subjects signed an informed consent approved by the AGAI or NYBB

For experiments involving mice, all experimental and surgical procedures were in accordance with the University of Chicago Animal Care and Use Committee guidelines. We used wildtype C57BL/6J mice housed on a 12hr light/dark cycle. Animals of either sex were used in all experiments and no sex-dependent differences were observed in any reported measures.

Human tissue preparation. One hemisphere from each of the embalmed specimens was used previously (Busch and Hansel 2023). Preparation of the vermis and opposing hemisphere from the embalmed specimens and of one hemisphere from the unembalmed specimens followed the same procedure as previously reported. In brief, whole cerebellums were fixed in 4% paraformaldehyde (PFA) for one week after being obtained, regardless of whether they were embalmed or unembalmed. Specimens were sectioned by hand in the parasagittal axis to obtain 3-5mm blocks that were sometimes cut transversely and further fixed for 2-4 days. Blocks were rinsed in 0.01M phosphate buffer saline (PBS) and sliced at 50µm in the parasagittal plane with a vibratome (Leica VT-1000S). Slices selected for immunolabeling were photobleached at 4°C for 3-4 days to reduce autofluorescence.

Mouse tissue preparation. To obtain sparse PC labeling for single cell dendrite and spine reconstruction in mice, we used tissue from animals expressing PC-specific GCaMP6f label for unrelated imaging studies. Surgeries were performed as described previously (Busch and Hansel 2023) on animals aged 10-12 weeks under ketamine/xylazine anesthesia (100 and 10mg/kg) with subcutaneous injections of meloxicam (1-2 mg/kg), buprenorphine (0.1 mg/kg), and sterile saline (0.5-1mL) as above. Body temperature was maintained at 35-37°C with a feedback dependent heating pad. The skin above the posterior skull was excised and the bone cleaned to implant a metal headframe over the interparietal bone via dental cement. After 3-4 days of recovery, mice were anesthetized and a 4mm craniotomy and durectomy was made at 2.5mm lateral from midline and 2.5mm caudal from lambda, exposing cerebellar simplex, crus I, and anterior crus II. A glass microelectrode with ~300µm tip diameter was used to inject a viral cocktail with low titer PC-specific L7-Cre (0.5%, AAV1.sL7.Cre.HA.WPRE.hGH.pA; Princeton Neuroscience Institute (PNI) Viral Core Facility; acquired from the lab of Dr. Samuel Wang, Princeton University) and high titer Cre-dependent GCaMP6f (20%, AAV.CAG.Flex.GCaMP6f.WPRE.SV40; Addgene, #100835) at a depth of ~300µm below the pial surface of lateral crus I (~900nL per site, 5min wait before needle retraction). A two-layer cranial window (4mm inner window, Tower Optical; 5mm outer window, Warner Instruments) was implanted over the craniotomy and sealed with dental cement (Metabond).

Imaging experiments were performed 2-3 weeks later, after which mice were anesthetized with ketamine/xylazine (100 and 10mg/kg) and perfused with 4% PFA. Sleep/wake periods may influence spine densities (Loschky et al., 2022), but we controlled for this in part by collecting mouse tissue during their sleep cycle, which may compare well with our human cases that passed away either during sleep or a period of decreased metabolism. Cerebellums were removed and incubated for 2hrs in 4% PFA at 4°C and then overnight in 30% sucrose in 0.1M PB at 4°C (until the tissue sank from the surface). The tissue was then rinsed briefly in 0.1M PB, dried and blocked, submerged in OCT medium, flash frozen, and then sliced (50µm, parasagittal plane) using a cryostat microtome (CM 3050S, Leica). Sparseness was not required to quantify cell morphology demographics across the vermis, so tissue was obtained from wildtype C57BL/6J mice without previous surgery and were anesthetized, perfused, and sliced as above.

Calbindin immunohistochemistry. Either unembalmed (for reconstructions) or embalmed (for regional analysis) tissue was washed in 50mM Glycine in 0.01M PBS for 2hrs at 4°C and incubated in 20mM Sodium Citrate in 0.01M PBS at 50-60°C using a heated water bath for 30min. After cooling to room temperature (RT), tissue was washed in 20mM Sodium Citrate for 5min then rinsed 2x30sec in dH20. Next, slices were permeabilized at RT in 0.01M PBS containing 0.025% Triton-X (PBS-TX) for 1hr. Blocking was done with PBS-TX containing 5% normal donkey serum (NDS) and 5% bovine serum albumin (BSA) for 1hr at RT followed by incubation in guinea pig anti-calbindin primary antibody (1:1000; Synaptic Systems Cat# 214 004, RRID:AB_10550535) solution overnight (18-20hrs) at 4°C with 1% normal donkey serum in PBS-TX. After 3x10min washes in PBS-TX at RT, slices were incubated in donkey anti-guinea pig Cy3 secondary antibody (1:200; Jackson ImmunoResearch Labs Cat# 706-165-148, RRID:AB_2340460) for 2hrs at 4°C with 1% NDS in PBS-TX. Finally, slices were washed in PBS-TX for 3x10min, mounted and coverslipped with Vectashield (Vector Laboratories, Inc.), and allowed to set overnight before visualization.

For calbindin based labeling of PCs in mouse tissue without GCaMP6f, the same procedure was used as above with some small changes: glycine incubation for 1hr instead of 2hrs and heated Sodium Citrate incubation for 20min instead of 30min. Slices were incubated in primary antibody solution with guinea pig anti-calbindin (1:1000), then in secondary antibodies with donkey anti-guinea pig Cy3 (both 1:200).

Dual calbindin and peripherin immunohistochemistry. VGluT2 and Cocaine- and Amphetamine-Regulated Transcript (CART) (Press and Wall 2008; Reeber and Sillitoe 2011) label CFs in human (Lin et al. 2014; Wu et al., 2021), but are restricted to terminal boutons and minor processes in the molecular layer, precluding disambiguation of mono- and multi-innervation without an olivary tracer (Miyazaki and Watanabe 2011; Busch and Hansel 2023). Some reports used Golgi impregnation to visualize human CFs (Ramón y Cajal 1909; Marin-Padilla 1985) but this technique cannot visualize CF-PC pairs in reliably beyond the molecular layer in post-natal tissue due to myelination. To distinguish fiber sources, we instead labeled CF axonal fibers with the intermediate neurofilament protein peripherin (Errante et al., 1998). Unembalmed human tissue was washed in 200mM Glycine in 0.01M PBS for 2hrs at RT and incubated in 10mM Sodium Citrate in 0.01M PBS at 80-90□ using a heated water bath for 30min. After cooling to RT, tissue was washed in 0.5% Tween-20 in 0.01M PBS (PBS-Tween) for 3x5min. Next, slices were permeabilized at RT in 0.01M PBS containing 2.5% Triton-X (PBS-TX) for 1hr and then incubated in 200mM Glycine in PBS-Tween for 15min. Blocking was done with PBS-Tween containing 10% normal donkey serum (NDS) and 5% bovine serum albumin (BSA) for 2hr at RT followed by incubation in polyclonal guinea pig anti-calbindin (1:500; Synaptic Systems Cat# 214 004, RRID:AB_10550535) and polyclonal rabbit anti-peripherin (1:500; EnCor Biotechnology Cat# RCPA-Peri, RRID: AB_2572375) primary antibody solution overnight (18-20hrs) at 4°C and then at RT for 3-4hrs with 1% normal donkey serum in PBS-Tween. After 3x10min washes in PBS-Tween at RT, slices were incubated in donkey anti-guinea pig AF488 (1:200; Jackson ImmunoResearch Labs Cat# 706-545-148, RRID:AB_2340472) and donkey anti-rabbit Cy3 (1:200; Jackson ImmunoResearch Labs Cat# 706-165-152, RRID:AB_2307443) secondary antibody solution for 2hrs at RT with 1% NDS in PBS-Tween. Finally, slices were washed in PBS-Tween for 3x10min, mounted and coverslipped with Vectashield (Vector Laboratories, Inc.) and allowed to set overnight before visualization.

Confocal imaging for cell, spine, and peripherin fiber reconstruction. Following immunolabeling of unembalmed human tissue and perfusion of GCaMP6f labeled mouse tissue, we selected PCs within L6-8 of the midhemisphere for their lack of truncation of their dendritic arbor and isolation from adjacent cells to minimize the chance of misattributing a branch from another cell. Cells and spines were then manually reconstructed using NeuronStudio (Rodriguez et al. 2003). No shrinkage factor or z-correction was applied.

Cell reconstructions: We collected z-stack tile scans of individual PCs at 40x (Zeiss EC Plan-Neofluar 1.3NA, oil immersion) with a confocal microscope (Zeiss LSM 900, Examiner.Z1) with 1x digital zoom, 2x line averaging, producing a 0.2079µm x 0.2079µm x 0.5µm voxel resolution.

Cell and peripherin fiber reconstruction: Multi-channel z-stack images of PCs and peripherin fibers were collected at 40x (Zeiss EC Plan-Neofluar 1.3NA, oil immersion; Zeiss LSM 900, Examiner.Z1) with 0.72x digital zoom, 2x line averaging, and 0.289µm x 0.289µm x 1µm voxel resolution.

Spine reconstruction: Single z-stack images of branch segments from distal, intermediate, and proximal compartments for spine reconstruction were collected at 63x (Leica HC PL APO 1.4 UV, oil immersion; Leica Stellaris 8 laser scanning confocal microscope; University of Chicago Integrated Light Microscopy Core RRID: SCR_019197) with 7x digital zoom, 4x line averaging, and 25.76nm x 25.76nm x 0.15µm voxel resolution.

Branch eccentricity was calculated by translating the origin of every branch to (0,0) in the coordinate plane and taking the slope of the best fit line for all branch trace vertices. The slope was mirrored over the x-axis for branches projecting downward toward the Purkinje cell layer (in quadrants 3 and 4 of the coordinate plane). As it made no difference whether the branch projected to the left or right, all branches projecting leftward (in the second quadrant of the coordinate plane) were mirrored over the y-axis for simplicity. Thus, the eccentricity of every branch relative to the horizontal plane of the Purkinje cell layer was maintained while the direction was reversed.

Each instance of an intact co-labeled PC and peripherin fiber allowed us to make one of four observations: "putative mono-innervation", in which a single fiber approaches the target PC and branches to run in apposition to all major primary dendrites (Fig. 3A); "absence multi-innervation", in which a single fiber approaches and runs in apposition with some primary dendrites but is conspicuously absent from others (Fig. 3B); "putative multi-innervation", in which the primary dendritic branches receive multiple unconnected fibers that are truncated so we could not observe their independence in the GCL (Fig. 3C); and "fully labeled multi-innervation", in which multiple labeled fibers approach the PC from the GCL and travel to distinct primary dendrites either entirely separately, or following a brief distance of shared apposition to a primary dendrite before diverging to different dendrites (Fig. 3D-E).

Slice reconstruction and cell counting. Parasagittal slices were traced and cells were mapped as described previously (Busch and Hansel 2023). Briefly, slides were visualized under 10x or 20x magnification (Zeiss Achroplan 0.25NA, air; Olympus UMPlanFL N 0.5NA, water) and illuminated with an epi-fluorescent light source (LEJ HBO-100). We manually scanned through the cerebellar cortex and classified Purkinje cells (PCs) by their dendritic morphology and their location by foliar sub-region (e.g. gyrus, bank, and sulcus), both based on criteria listed below. To mark the morphology and cell location accurately in both human and mouse tissue, we initially traced the outlines of the pial surface, white matter tracts, and PC layer of the whole parasagittal section. Cells were only included for categorization if the soma and at least 200µm lengths of primary dendritic trunks were clearly labeled such that all features of Normative, Split, and Poly and vertical or horizontal categories were unambiguously present or absent (see criteria below). We marked the location and morphological type of each cell in the slice map and scanned this map as an input image to a custom Matlab GUI where each point's X,Y coordinate, foliar location, and morphological category could be digitized. The output data were imported to R for downstream analysis and plotting.

Purkinje cell morphological category definitions and criteria. Criteria for morphology category definitions were the same as previously (Busch and Hansel 2023) but we reiterate the full description here for clarity. In human, PCs were deemed Normative if they had the following features: 1) a single trunk emerging from the soma, and 2) either no bifurcation of the primary trunk within two soma distances (2x the diameter of the soma, 25-35µm per soma) or a highly asymmetrical bifurcation where the smaller branch did not project in the parasagittal axis more than 200µm from the main dendritic compartment. PCs were defined as Split if they had the following features: 1) a single trunk emerging from the soma, and 2) either symmetrical bifurcation of the primary trunk within two soma distances or an asymmetrical bifurcation within two soma distances where the smaller branch projected more than 200µm from the main dendritic compartment and thus reached prominence by its overall length and sub-branching. PCs were defined as Poly if they had more than one trunk emerging from the soma regardless of relative size.

In mouse, PC categories were defined the same way, except that the bifurcation threshold of two soma distances (each soma diameter is 18-22µm) was set at 40µm, and the smaller branch of an asymmetrical bifurcation had to project only 100µm away from the main dendritic compartment.

In mouse and human, Split and Poly PCs were further subdivided into Vertical or Horizontal ramification patterns. Split and Poly PCs were defined as Horizontal if one of two primary dendrites ramified parallel with the PC layer for >300µm in human (>150µm in mouse), or both primary dendrites ramified in opposing directions parallel with the PC layer for >150µm each in human (>75µm in mouse). Dendrites were considered parallel if the dendrite, at 300 or 150µm from the soma respectively, ramified at <30° from the top of the PC layer. Otherwise, the cell was defined as Vertical.

Foliar sub-region category definitions and criteria. Criteria for foliar category definitions were the same as previously (Busch and Hansel 2023) but we reiterate the full description here for clarity. Purkinje cell locations were defined as either Gyrus, Bank, or Sulcus based on the relative expansion/compression of the granule cell/molecular layers in the parasagittal axis. Gyrus was defined as a region where the total parasagittal length of the pial surface exceeded that of the border between the granule cell layer and the white matter. Bank was defined as regions where those two lengths were equal, such that neither layer of the cortex was compressed or expanded relative to the other. Finally, Sulcus was defined as regions where the total parasagittal length of the pial surface was less than that of the border between the granule cell layer and the white matter. Both intermediate sulci, embedded within a continuous Bank region, and full sulci were combined for these analyses.

Spine morphology criteria, and volume calculations. Manual reconstruction of spines was performed using NeuronStudio and by scanning through a z-stack image of a spiny branch to better visualize the relations between contiguous and sometimes non-contiguous structures surrounding the dendrite. Spines were categorized as either thin or mushroom spines if they had a classical head and neck structure with a head that had either a less than or greater than 500nm diameter, respectively. Spines were categorized as branched if two heads emerged from a shared neck emerging from the dendrite. Spines were categorized as ‘spine clusters’ if they had a single head with discontinuous and/or bumpy structure that produced three or more puncta with distinct prominences from the core head matrix.

Spine volume as a fraction of volume surrounding the dendrite was calculated by taking the sum of the spine head volumes for each branch segment and dividing it by the volume of the surrounding cylindrical space, which in turn was the subtraction of the cylindrical volume of the dendrite (using the mean dendritic radius) from the larger cylindrical volume with a radius combining the mean dendrite radius and the mean spine head protrusion distance.

Cell morphology clustering analysis. The output dataset from slice reconstruction and cell counting contained cell ID information paired with X,Y coordinates in the slice. To calculate cell type clustering, we wrote a custom R script to measure cluster scores for each cell based on either immediately adjacent cells or cell populations.

Adjacency clustering: First, for each dataset (one slice each from vermis and the mid-hemisphere for each individual), the Euclidean distance was calculated between each consecutive pair of cells along the PC monolayer from anterior to posterior. Second, an initial cluster score of -1 was assigned to each cell. Third, the final cluster score was assessed for each cell based on whether the leading or following immediately adjacent cell matched the morphology of that cell. If there were adjacent cells within the threshold distance (1000µm for human, 200µm for mouse), then the cluster score was set at 0. Leading or following adjacent cells with matching morphologies each added (+1) to the cluster score, producing either a final score of 1 if one of two adjacent cells match or 2 if both are matching. The morphology match was determined one of several different ways, requiring either a complete match (e.g. both the morphological type of Normative, Split, or Poly and the orientation of vertical or horizontal are the same; thus, cells fall into five total categories of Normative, vertical Split, horizontal Split, vertical Poly, and horizontal Poly, wherein a vertical Split cell does not match with a horizontal Split cell or a vertical Poly cell), or a more liberal match by only morphological type (e.g. Normative,

Split, or Poly; thus, a vertical Split cell matches with a horizontal Split cell but not a vertical Poly cell) or orientation (e.g. vertical or horizontal; thus, a vertical Split cell does not match with a horizontal Split cell but does match a vertical Poly cell). Once cluster scores were calculated, consecutive IDs were assigned to each cluster such that the number of cells and total parasagittal inter-somatic distance could be determined. The identical operation was performed for a shuffled version of each dataset to compare the observed effect of clustering with chance based on cell type ratios. All aspects of cell information were held constant (e.g. X,Y coordinate, location by foliar sub-division) and the morphology was shuffled without replacement (i.e. the same ratio of cell types was maintained). To assess the specific effect of foliar location on clustering, the same analysis was performed but using a shuffled dataset in which the possible shuffled cell type identities for each cell was only drawn from the cells within the same foliar sub-division (e.g. gyrus, bank, or sulcus).

Population clustering: Here, the number of cells of every type was tallied among the whole population of cells within a defined distance of each cell in question. This threshold varied from 250µm and 50µm in human and mouse, respectively, to 10mm and 2mm, respectively. Thus, this analysis is more lenient to interruptions in an otherwise relatively homogeneous population by assessing multiple cells and not just the single most adjacent leading and following cells. The frequency of observing each cell type in the population around each cell type was determined. From that was subtracted the same calculation for a version of each dataset that was shuffled as described above without considering foliar location (e.g. new shuffled identities were drawn from the whole population, not just from those cells in the same foliar sub-division). This subtraction gave us a percent relative increase in the rate of observing either the one complete matching morphology, or any of all four non-matching morphologies, versus the rate expected by chance. Then, across all cell types, we averaged the rates of all matches (e.g. combining the rate of vertical Splits near a vertical Split with the rate of horizontal Polys near horizontal Polys, etc.) and non-matches (e.g. combining the rate of vertical Splits near a horizontal Polys with the rate of vertical Polys near Normative, etc.).

When measuring wider populations with larger radius thresholds, we controlled for the effect of local clustering on the rate of clustering among distant cells by instead assessing cell populations selectively in 500µm leading and following shell regions around each cell while ignoring the most immediately local cells within the core region (from the soma location to the inner edge of the shell analysis region) around the cell in question. For example, to analyze clustering in a 500-1000µm shell region, we only included cells that were at least 500µm away but no more than 1000µm away on either side (leading and following the cell in question), and thus ignored more local cells within a core 1000µm (500um on either side) of the cell in question. Similarly, to analyze clustering in a 1500-2000µm shell region, we only included cells that were at least 1500µm away but no more than 2000µm away on either side (leading and following), and thus ignored more local cells within a 3000µm core region around the cell. By calculating the elevation of clustering over chance for equivalently sized shell regions with variable distances running step-wise in 500µm increments while ignoring a growing core region, we could selectively isolate distant populations and observe the true drop-off distance for clustering.

Statistics. Standard parametric statistics such as the Students' T-test or ANOVA with Tukey post-hoc and Bonferroni correction were used to assess individual and multi-group comparisons except in cases where the data were non-normally distributed, in which case we used single or multiple comparisons Mann-Whitney U tests. In cases of a paired comparison where the underlying inter-individual variability was uninformative, we performed a one-way Students' T-test on within-individual normalized data. A Kolmogorov-Smirnov test was used to assess differences between cumulative distributions. A Chi-squared test for independence was used to distinguish the ratios of categorical data by group. Co-variation of each measure by sex was assessed but no significant differences were observed.

Methods References

Errante, L. et al. The intermediate filament protein peripherin is a marker for cerebellar climbing fibres. J Neurocytol 27, 69–84 (1998).

Marin-Padilla, M. Neurogenesis of the climbing fibers in the human cerebellum: A Golgi study. Journal of Comparative Neurology 235, 82–96 (1985).

Miyazaki, T. & Watanabe, M. Development of an anatomical technique for visualizing the mode of climbing fiber innervation in Purkinje cells and its application to mutant mice lacking GluRδ2 and Cav2.1. Anat Sci Int 86, 10–18 (2011).

Press, D. A. & Wall, M. J. Expression of cocaine- and amphetamine-regulated transcript (CART) peptides at climbing fibre-Purkinje cell synapses in the rat vestibular cerebellum. Neuropeptides 42, 39–46 (2008).

Reeber, S. L. & Sillitoe, R. V. Patterned expression of a cocaine- and amphetamine-regulated transcript peptide reveals complex circuit topography in the rodent cerebellar cortex. Journal of Comparative Neurology 519, 1781–1796 (2011).

Rodriguez, A. et al. Automated reconstruction of three-dimensional neuronal morphology from laser scanning microscopy images. Methods 30, 94–105 (2003).

Figure 1. Cell reconstructions reveal expanded dendritic size and compartmentalization of human PCs. A-B) Manually reconstructed human and mouse PCs (same scale). **C)** Meta-analysis of historical measures of mean±sd total dendritic length in human (dark grey) and mouse (light grey) compared with that reported here for human (blue) and mouse (green) (values in D). **D-I)** Total dendritic length, number of branches, maximum terminal branch order, maximum width and height of the dendritic arbor, and numerical index for the shape of the dendritic area by morphological category (N—Normative, S—Split, P—Poly; positive values indicate arbors with greater width than height; n = 5,5 cells, 3,2 individuals). Cells pictured in A-B are highlighted by colored outlines according to morphology (Normative=Yellow, Split=Green, Poly=Purple). **J)** Schematic calulation of branch segment eccentricity relative to cortical depth and the PC layer (PCL) plane (top). Eccentricity data for all branches on quarter-radial plots (middle; black arrows are population mean) and as distributions with cell averages (bottom) by categories of distance from the soma (proximal, intermediate and distal thirds of ML thickness) in human and mouse (ANOVA, Tukey's HSD post-hoc; n = 2749,7595,2541 and 877,1247,1056 branches). **K)** Maximum diameter of the primary dendrite (or dendrites for Poly PCs). **L)** Dendrite diameter normalized to the thickest primary dendrite by order. **M)** Distribution of all branch diameters. **N)** Cumulative distribution of branch segments by their diameter relative to the thickest dendrite. (Kolmogorov-Smirnov test; n = 5,5 cells). **O)** Percent of the total dendritic length classified as thin caliber using a 1.31um threshold (log-normal mean + 1sd of all branch thicknesses across species (Student's t-test; n = 5,5 cells). **P)** Branch segment lengths (Mann-Whitney U test; n = 12885,3180 branches). **Q)** Cumulative (top) and non-cumulative (bottom) normalized distributions of dendritic length by centrifugal Sholl distance from the soma (Kolmogorov-Smirnov test, n = 5,5 cells). **R)** Total dendritic length at each 1μm Sholl radius without normalization.

Figure 2. Human PCs host expanded sites for putative input and spines with complex morphology. A) Example 3D reconstructions of human and mouse spiny dendrites (background removed for clarity) with inset schematic of spine types: thin (solid arrowhead), mushroom (open arrowhead), branched (back-to-back arrowheads), cluster (star). **B)** Density of all spines (left) and by spine type in human and mouse (n = 15,12 branches). **C)** Spine densities by branch location relative to the soma (Student's paired one way t-test for promixal vs distal compartments; n = 5,4 cells) **D)** Spine head diameters of thin and mushroom spines (Student's t-test; n = 2066,1246 spines). **E)** Spine neck length by species (Student's t-test; n = 2323,1376 spines). **F)** Ratio of spine head volume to volume surrounding the dendrite (Student's t-test; n = 15,12 branches). **G)** Spine head diameter by branch location (ANOVA, Tukey's HSD post-hoc; n = 345,478,424 spines in human, 676,767,812 in mouse). **H)** Spine to surround ratios by branch location (n = 4,4 branches). **I)** Example spine cluster with enlarged neck diameter and spine head. **J)** Spine cluster density, included in the total density in **(B**, left**)**. **K)** Spine cluster density by branch location, included in the total density in **(C**, left**)** (Student's one way t-test for promixal vs distal compartments; n=5 individuals). **L)** Number of puncta per cluster by branch location (n = 46,67,76 spines). **M)** Spine cluster head volume by branch location (n = 46,67,76 spines). **N)** Spine cluster diameter as a function of puncta number (n = 189 spines). Blue points are means by puncta number. **O)** Total puncta across spine clusters on each branch segment by location and normalized to the proximal branch (Student's one way t-test for promixal vs distal compartments; n = 5 individuals).

Figure 3. Peripherin and calbindin dual-labeling reveals non-canonical CF multi-innervation of adult human PCs. A) Example reconstruction from human of a PC and peripherin-labeled fiber as originally traced (left) and with masks drawn for visualization (right) to exemplify putative mono-innervation. **B)** Example PC and peripherin-fiber masks to exemplify absence multi-innervation. **C)** Example of putative multi-innervation. **D)** Examples of fully labeled multi-innervation. **E)** A Poly PC with multiple peripherin fibers of varying thickness approaching separate dendrite compartments from distinct locations in the granule cell layer. Untraced composite PC and peripherin-fiber images (top, center) with separate (top, outside) and combined (bottom) masks of each primary dendrite. **F-G)** Distribution of cell types **(F)** and orientations **(G)** by peripherin fiber classification (n = 2 individuals, 44 cells). Numbers above bars indicate absolute counts.

Figure 4. Regional and locally clustered PC demographics in the vermis of human and mouse. A) Example exhaustive reconstruction of PC morphological distributions in a parasagittal section of human vermis. **B)** Morphological orientation (top) and type (bottom) demographics across lobules (Chi-squared test; n = 3 individuals, 6346 cells). **C)** Example exhaustive reconstruction of a parasagittal section from mouse vermis. **D)** Morphological type (top) and orientation (bottom) demographics across lobules in mouse (Chi-squared test; n = 3 individuals, 2284 cells). **E)** Observed and shuffled rates of adjacent PC clustering in human and mouse (within species ANOVA, Tukey's HSD post-hoc; n = 3 individuals and 20 shuffles of each). Numbers between graphs indicate the difference between observed and shuffled mean. * $p < 0.05$, ** $p < 0.01$, *** $p < 0.005$.

Figure 5. Adjacent and local non-random cell type clustering in human and mouse vermis. A) Schematic of cluster score assignment based on complete morphological match (left) and score use to identify the number of cells and parasagittal length of clusters (right). **B-C)** Number of cells **(B)** and length **(C)** of PC clusters in mouse and human compared to shuffled data (Mann-Whitney U test; n = 288,1295 observed clusters; n = 263,1122 shuffled clusters). **D)** Schematic of local population demographics measured over variable distances (top). Radii in mouse are 20% the length in human, matching the difference in dendritic width. Rates of matching (dark points) and non-matching (light points) morphologies in a shuffled population are subtracted from unshuffled data to measure the percent elevation of clustering in human and mouse. Points mark the average demographic difference between observed and shuffled rates across all five cell groups (i.e. one dark point represents the average for matching cell rates of Normative to Normative, Split to Split, etc.). **E)** To measure the absolute spatial scale of elevated PC clustering, we measure the observed vs shuffled rate for 500µm increments of a shell region around a growing core. By ignoring the morphologies of the core region, we exclude local clustering from measurements of distant clustering.

Figure 6. Inter-hemisphere similarity of PC demographics is congruent with functional lateralization. A) Schematic of human cerebellum. **B)** Parasagittal reconstructions of PC morphological distributions in left and right mid-hemisphere lobules L5-Crus II within the same individual. **C)** Morphological demographics across lobules in left (top) and right (bottom) hemispheres by individual. **D)** Absolute differences of morphological demographics across hemispheres by lobule and individual. **E)** Normalized mean inter-hemisphere demographic difference from L6 by lobule and individual (Student's one-way t-test; n = 3 individuals).

Figure S1. All manual cell reconstructions. A) Example confocal tile scan (top left) and resolution of each individual image (below) with manually reconstructed human PCs. **B)** Manually reconstructed mouse PCs. Cells throughout are at the same scale.

Figure S2. Additional morphological data from digital reconstructions. A) Number of branch points by species. **B)** Maximum number of branch points, regardless of whether the branching is symmetrical or reduces diameter such as would define a change in dendrite caliber, between the terminal segments and the soma. **C)** Number of primary dendrite compartments, defined as the number of thick dendritic sections giving rise to only thin caliber branches, by the morphological category of each reconstructed PC. **D)** Distribution of branch eccentricities as a function of branching order for each reconstructed PC. **E)** Somatic diameters. **F)** Mean branch diameter by order. **G)** Distribution of total branch segments in each branching order. A reference symmetrical fractal pattern is represented by the function $y=2^{x+1}$ (black line). The right panel zooms in on the early branching orders. **H)** Distribution of mean dendritic length across branches of each order. **I)** As in **(F)** but normalizing for maximum branch order. **J)** Distribution of terminal branch segment lengths (Mann-Whitney U test; n = 6883,1773 branches). **K)** Branch distances from the soma (Mann-Whitney U test; n = 12885,3180 branches). **L)** Distribution of branch segments by branch order as in Fig. 1M but without normalizing segment number across species. **M)** Distribution of branch points by normalized Sholl distance from the soma.

Figure S3. Additional data from digitally reconstructed spines. A-B) Example 3D reconstructions of mouse (A) and human (B) spiny dendritic branches. Images in B1 are from one 93yo specimen while images in B2 are from one 37yo. All images on the same scale. **C)** Diameter of all dendritic banches reconstructed in this study.

Lines connect the compartments across each cell (n = 4,5 individuals). **D)** Distributions of spine neck lengths by location and species. **E)** Distribution of spine neck lengths by spine type and species. **F)** Spine protrusion distance, measured from the edge of the dendritic shaft to the distal tip of the spine head, in human and mouse (ANOVA, Tukey's HSD; n = 720,818,862 spines, n = 376,528,476 spines). **G)** Spine head diameter by spine type and location in mouse (top) and human (bottom). **H)** Spine head volume by spine type and location in mouse (top) and human (bottom).

Figure S4. Human PCs with multi-branched and horizontally oriented morphology can avail themselves of additional branch specific capacities. A) Example masks from a digitally reconstructed PC (grey) and peripherin fiber (blue) on which two unconnected calbindin(+) PC axons (dark and light green) converge to innervate distinct dendritic compartments. **B)** Example z-projections of two horizontally oriented Poly PCs hosting axons that emerge from the dendrite or an intermediate zone between somatic and dendritic compartments (orange arrowheads).

Figure S5. Additional reconstructions and analysis of PC demographics in parasagittal slices of vermis from human and mouse. A-B) Parasagittal human and mouse vermis reconstructions demonstrating the spatial distributions of each morphological type. **C)** Schematic of foliar subdivisions into gyrus, bank, and sulcus (top) and the demographics of PC types by foliar area (bottom). **D)** Demographics of PC orientations by foliar area. **E)** Observed versus shuffled rate of PCs having the same morphologyical classification by cell type (as if Fig. 4E) when the shuffled data are constrained within foliar subdivision. Numbers between graphs indicate the difference between observed and shuffled mean. **F-G)** Matrices of all cell type-by-cell type clustering likelihoods observed in the original data (top) and in the shuffled dataset (bottom) and separated by foliar area in human and mouse (N—Normative, S—Vertical Split, P—Vertical Poly, SS—Horizontal Split, SP—Horizontal Poly). * $p < 0.05$, ** $p < 0.01$, *** $p < 0.005$.

Figure S6. Adjacent PC demographics reveal the spatial scale of non-random morphological clustering among local PCs. A) Schematic of cluster score assignment for each PC based on whether the morphology of adjacent cells (<1000um away) matches (left) and the use of these scores to identify the number of PCs and parasagittal length of clusters of redundant cell types (right). **B)** Number of cells (top) and length (bottom) of PC clusters with identical morphology (complete match with five cell categories: Normative, vertical Split, vertical Poly, horizontal Split, horizontal Poly) in mouse and human with that of shuffled data in which morphologies are randomly resorted while cell locatiuon is held constant. **C-D)** As in **(B)**, but for PC clusters with only a partial match based on cell type (Normative, Split, or Poly; for example, vertical and horizontal Split PCs are a match) or cell orientation (Vertical or Horizontal; for example, horizontal Split PCs and horizontal Poly PCs are a match). **E-G)** As in **(B-D)** for PCs in slices from mid-hemisphere.

Figure S7. Population PC demographics reveal the spatial scale of non-random morphological clustering among parasagittal PC circuits. A) Schematic of how various radius distances are used to survey the demographics of all cells within a given distance from a PC (top). Radii used in the mouse are set to 20% that of the human, matching the difference in the width of a mouse vs human PC. The rate of PCs with matching morphology (using a complete match across five categories) is compared with the same measurement of shuffled data to generate a difference between the observed vs shuffled percents of cells with a matching morphology (dark points) compared to non-matching morphologies (light points) in human and mouse (bottom). Points mark the average demographic difference between observed and shuffled rates across all five cell groups (i.e. one dark point represents the average for matching cell rates of Normative to Normative, Split to Split, etc.). **B)** To measure the absolute spatial scale of elevated PC clustering, we measure the observed vs shuffled rate for 500um increments of a shell region around a growing core. By ignoring the morphologies of the core region, we control for the effect of highly local clustering on the measurement of more distant PCs. This reveals that non-random morphological clustering appears to drop off at distances of ~1500um and 300um in human and mouse, respectively.

Figure S8. Additional reconstructions and analysis of PC demographics in parasagittal slices of the mid-hemisphere of human. A-B) Parasagittal reconstructions of lobules 5-Crus II of the opposing hemispheres of human specimens used previously, demonstrating the spatial distributions of each morphological type. **C)** Distribution of PCs across lobules of the mid-hemisphere by cell orientation (as in Fig. 4B). **D)** Observed versus shuffled rate of adjacent PCs having the same morphologyical classification by cell type in human (top) and mouse (bottom). Numbers between graphs indicate the difference between observed and shuffled mean. **E)** As in **(D)**, but with shuffled morphologies being constrained within foliar subdivision (e.g. PCs in the sulcus are only shuffled among each other, not also with PCs in the bank or gyrus). **F-G)** Matrices of all cell type by cell type clustering likelihoods observed in the original data (top) and in the shuffled dataset (bottom) and separated by foliar area in human and mouse (N—Normative, S—Vertical Split, P—Vertical Poly, SS—Horizontal Split, SP—Horizontal Poly). * $p < 0.05$, ** $p < 0.01$, *** $p < 0.005$.

Figure S9. Human cerebellar regional borders as defined by morphological demographics or functional imaging. The top and bottom rows provide four regional sub-divisions according to either involvement in behavioral tasks[49] or PC morphological demographics. The middle row indicates the lobules corresponding to both the above functional and below morphological sub-divisions.

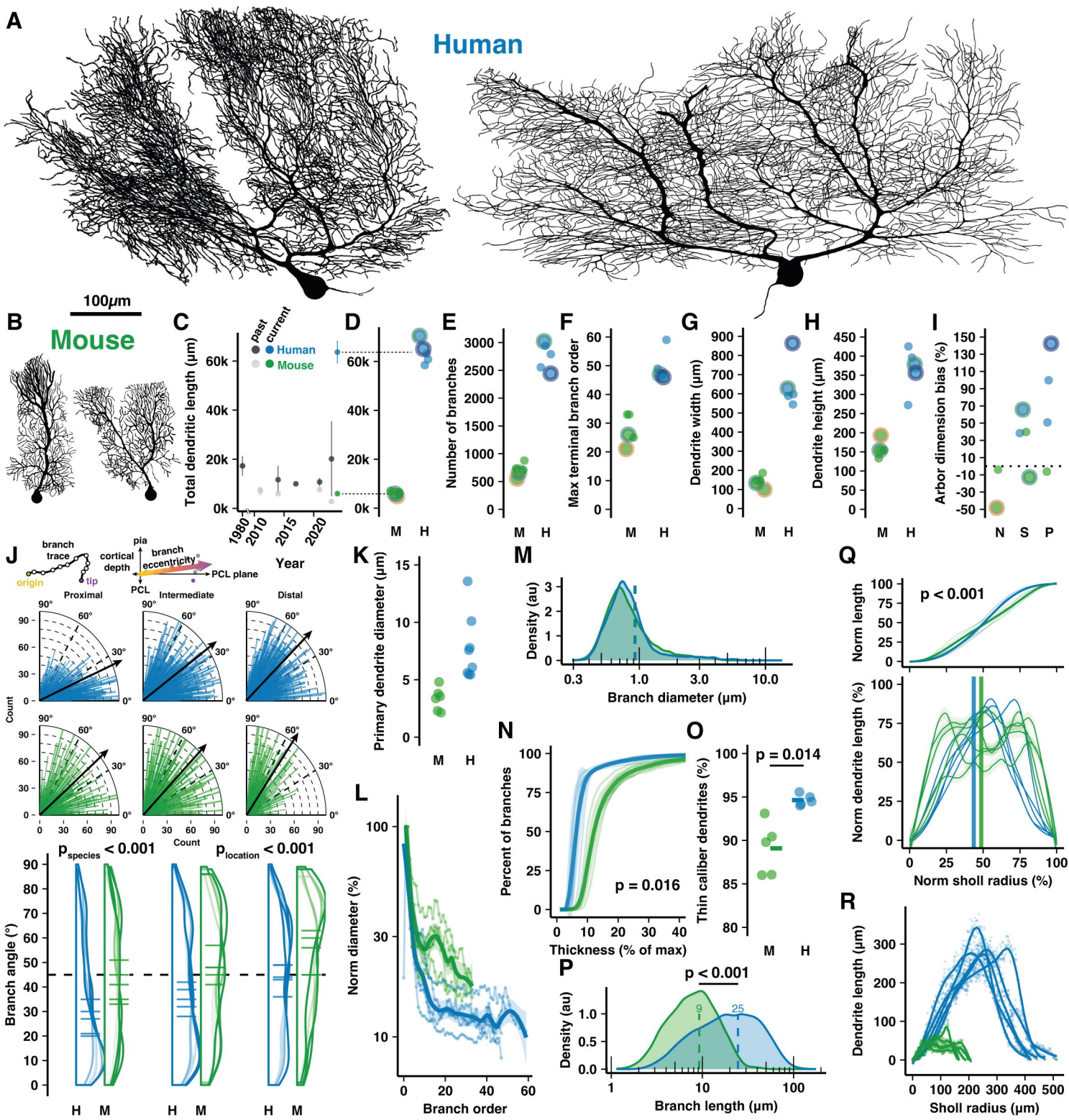
A
Human
100μm
B
Mouse
C
past
current
Human
Mouse
Total dendritic length (μm)
Year
D
E
Number of branches
F
Max terminal branch order
G
Dendrite width (μm)
H
Dendrite height (μm)
I
Arbor dimension bias (%)
M
H
N
S
P
J
branch trace
origin
tip
pia
cortical depth
branch eccentricity
PCL plane
PCL
Proximal
Intermediate
Distal
Count
K
Primary dendrite diameter (μm)
L
Norm diameter (%)
Branch order
M
Density (au)
Branch diameter (μm)
N
Percent of branches
Thickness (% of max)
p = 0.016
O
Thin caliber dendrites (%)
p = 0.014
P
p < 0.001
Branch length (μm)
Q
Norm length
Norm dendrite length (%)
Norm sholl radius (%)
R
Dendrite length (μm)
Sholl radius (μm)
p_species < 0.001
p_location < 0.001
Branch angle (°)

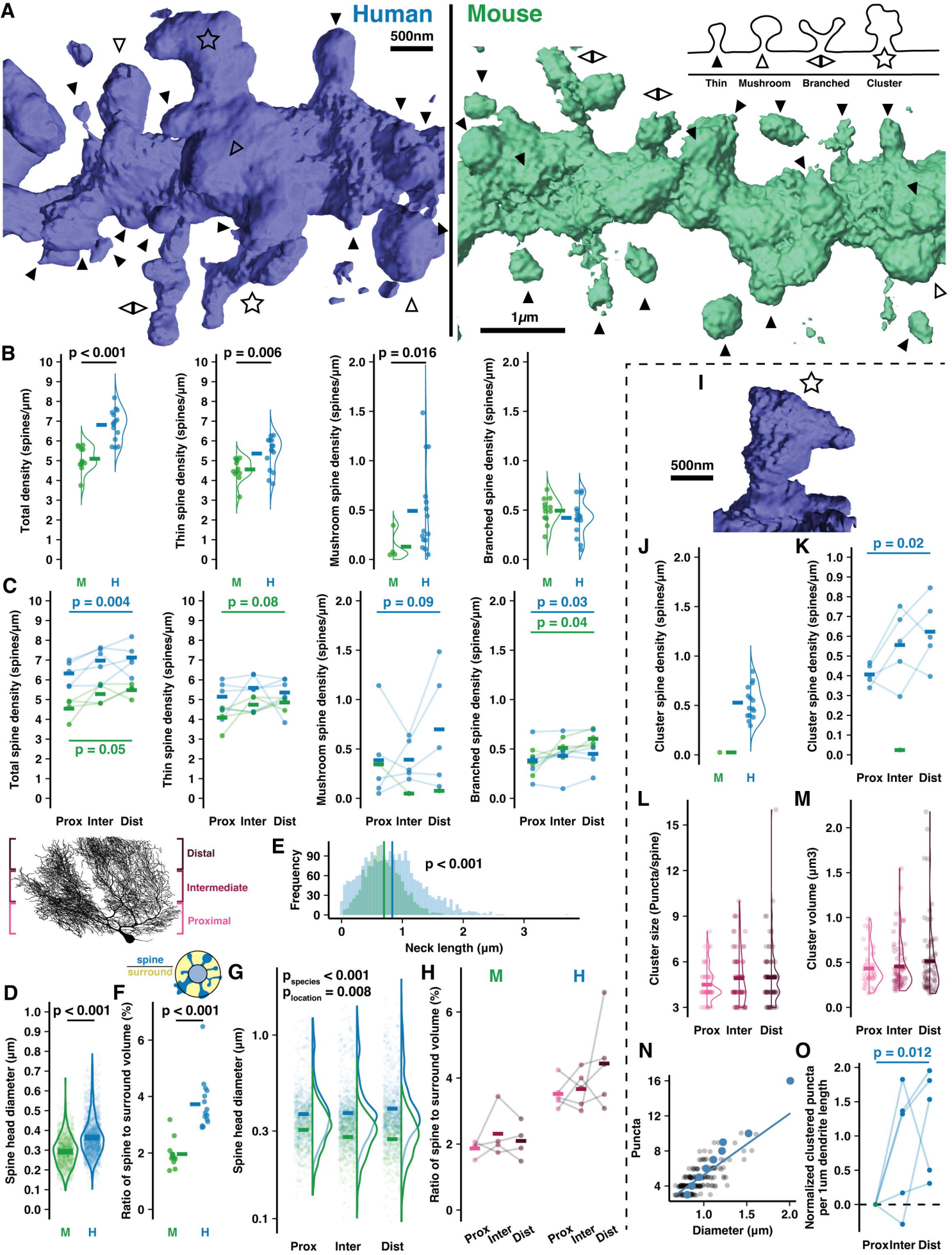
A
Human
500nm
Mouse
Thin
Mushroom
Branched
Cluster
1μm
B
p < 0.001
p = 0.006
p = 0.016
Total density (spines/μm)
Thin spine density (spines/μm)
Mushroom spine density (spines/μm)
Branched spine density (spines/μm)
M
H
C
p = 0.004
p = 0.05
p = 0.08
p = 0.09
p = 0.03
p = 0.04
Total spine density (spines/μm)
Thin spine density (spines/μm)
Mushroom spine density (spines/μm)
Branched spine density (spines/μm)
Prox Inter Dist
Distal
Intermediate
Proximal
E
Frequency
p < 0.001
Neck length (μm)
spine
surround
D
p < 0.001
Spine head diameter (μm)
F
p < 0.001
Ratio of spine to surround volume (%)
G
$p_{species}$ < 0.001
$p_{location}$ = 0.008
Spine head diameter (μm)
H
Ratio of spine to surround volume (%)
I
500nm
J
Cluster spine density (spines/μm)
K
p = 0.02
Cluster spine density (spines/μm)
L
Cluster size (Puncta/spine)
M
Cluster volume (μm3)
N
Puncta
Diameter (μm)
O
p = 0.012
Normalized clustered puncta per 1um dendrite length

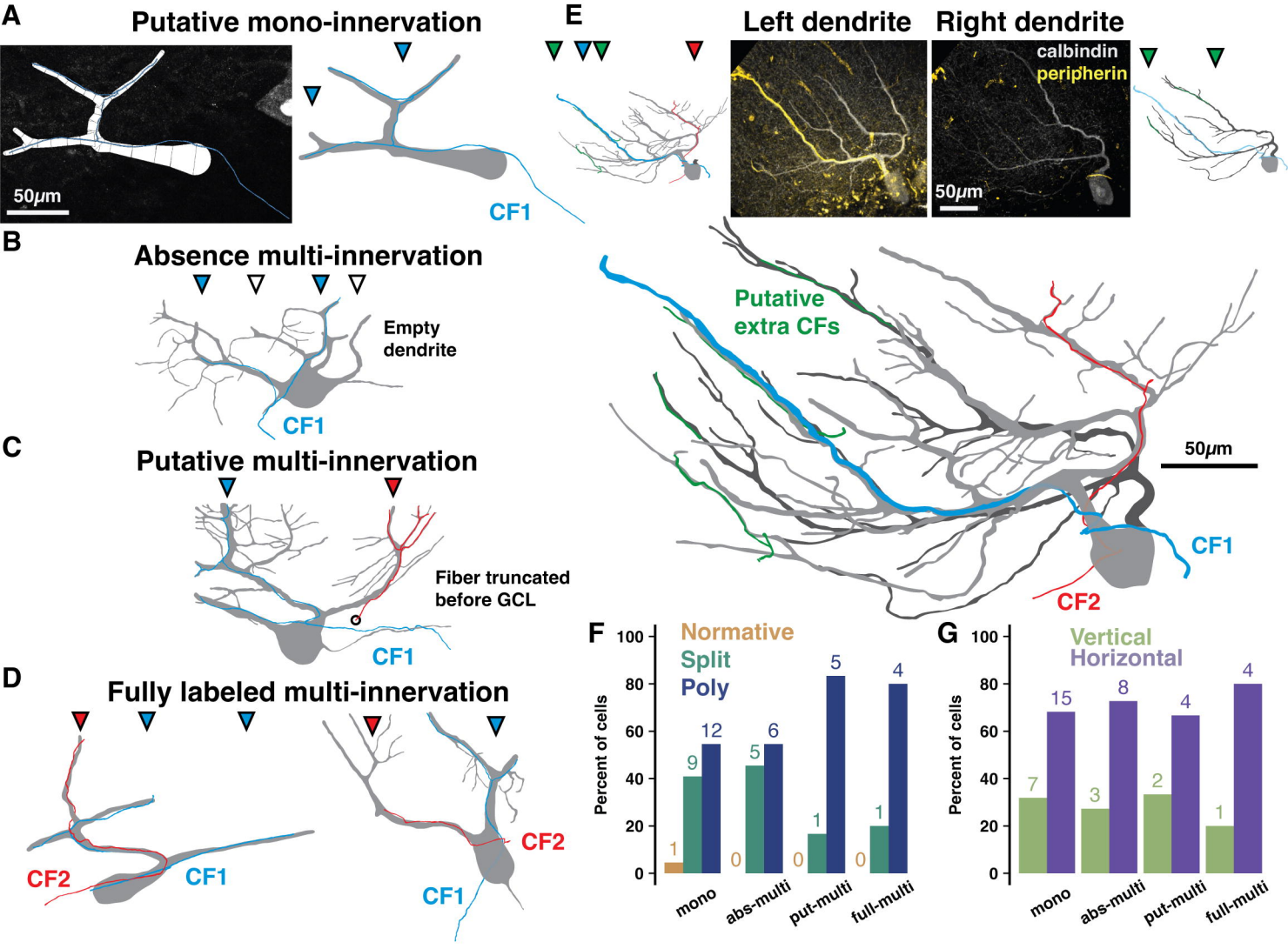
A
Putative mono-innervation
50μm
CF1
B
Absence multi-innervation
Empty dendrite
CF1
C
Putative multi-innervation
Fiber truncated before GCL
CF1
D
Fully labeled multi-innervation
CF2
CF1
CF2
CF1
E
Left dendrite
Right dendrite
calbindin
peripherin
50μm
Putative extra CFs
50μm
CF1
CF2
F
Normative
Split
Poly
Percent of cells
mono
abs-multi
put-multi
full-multi
G
Vertical
Horizontal
Percent of cells
mono
abs-multi
put-multi
full-multi

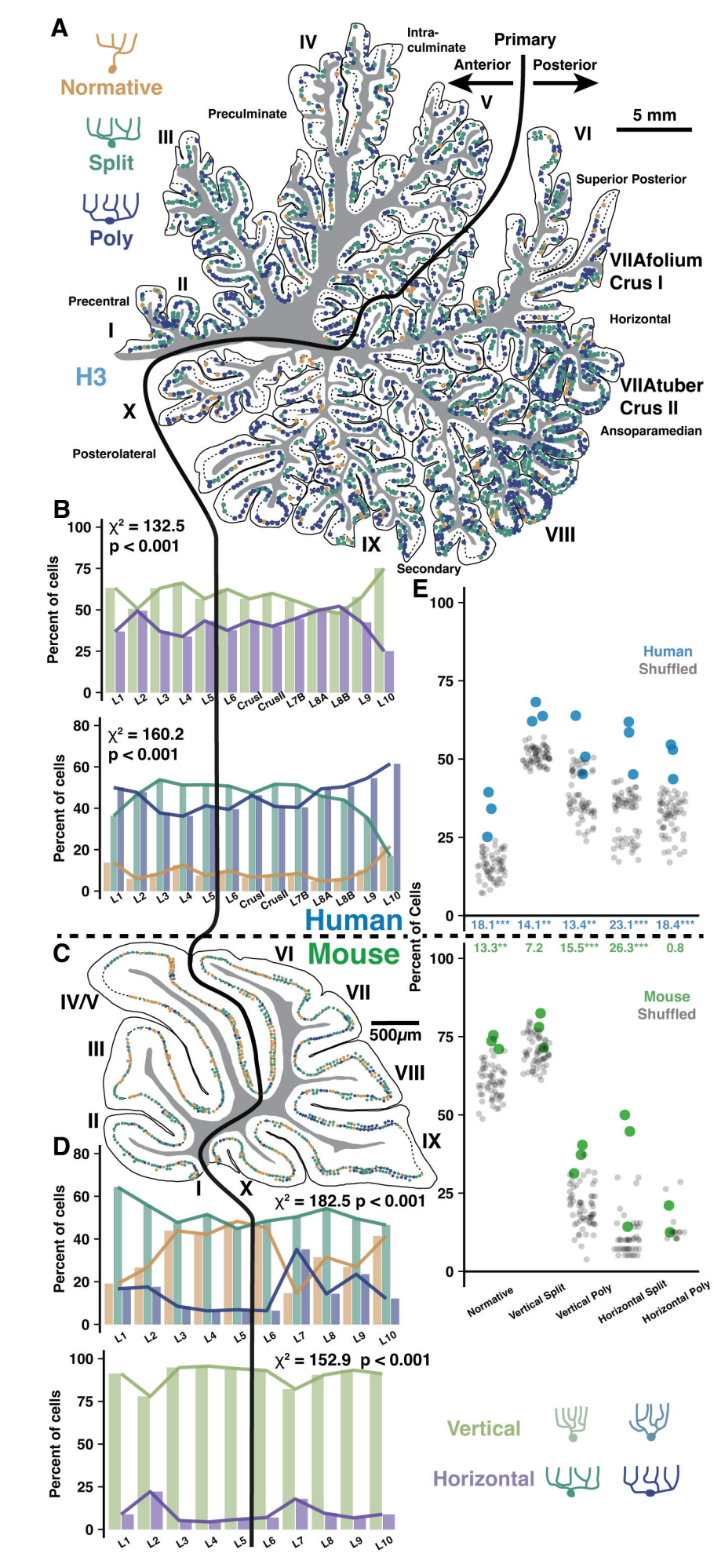
A
Normative
Split
Poly
H3
Primary
Anterior
Posterior
Intra-culminate
Preculminate
Precentral
Superior Posterior
VIIAfolium Crus I
Horizontal
VIIAtuber Crus II
Ansoparamedian
Posterolateral
Secondary
5 mm
I
II
III
IV
V
VI
VII
VIII
IX
X
B
χ² = 132.5
p < 0.001
χ² = 160.2
p < 0.001
Percent of cells
L1 L2 L3 L4 L5 L6 CrusI CrusII L7B L8A L8B L9 L10
Human
C
Mouse
IV/V
500μm
D
χ² = 182.5 p < 0.001
χ² = 152.9 p < 0.001
E
Human
Shuffled
Percent of Cells
18.1*** 14.1** 13.4** 23.1*** 18.4***
13.3** 7.2 15.5*** 26.3*** 0.8
Mouse
Shuffled
Normative
Vertical Split
Vertical Poly
Horizontal Split
Horizontal Poly
Vertical
Horizontal

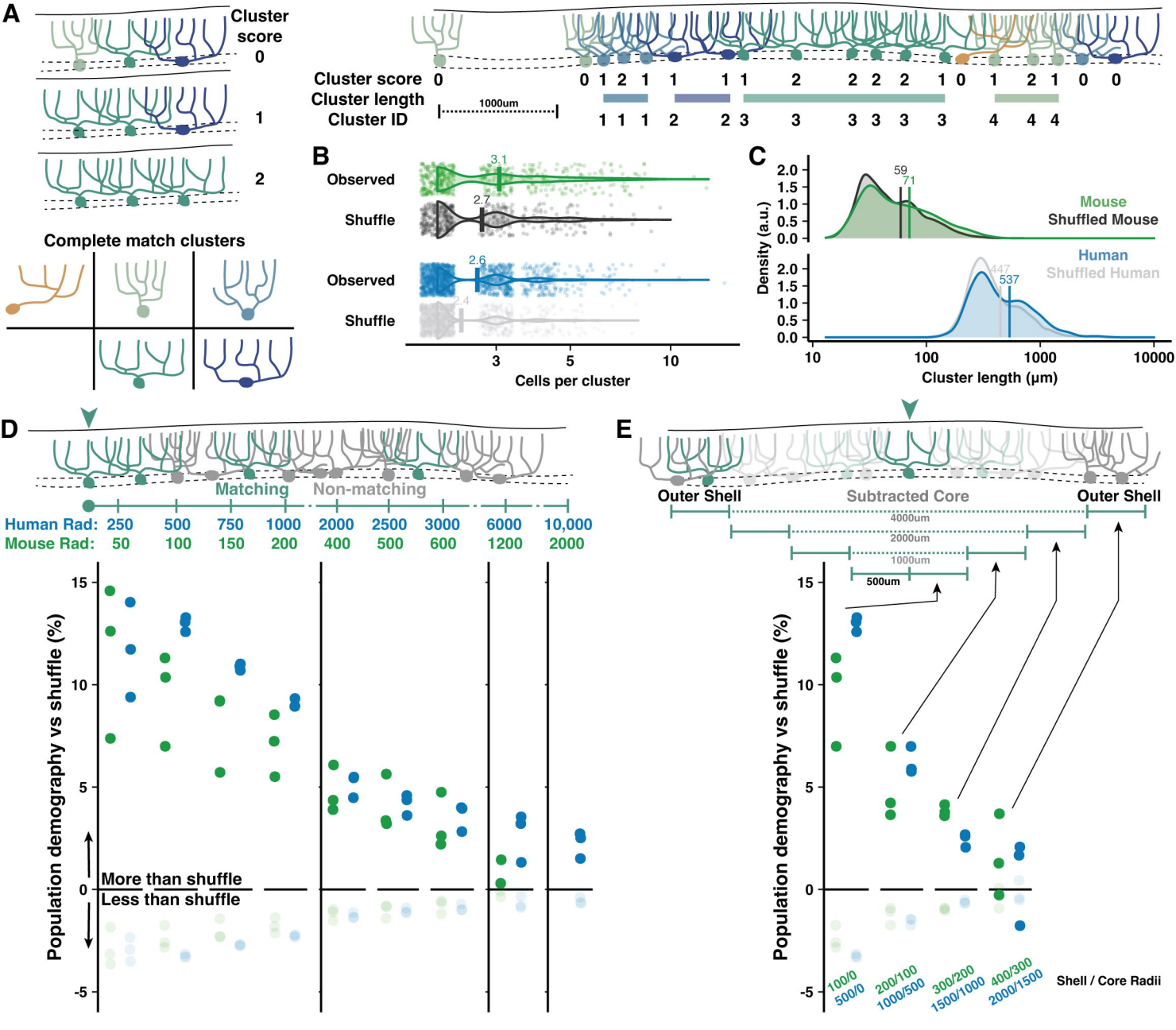
A
Cluster score
0
1
2
Complete match clusters
Cluster score 0 0 1 2 1 1 1 1 2 2 2 2 1 0 1 2 1 0 0
Cluster length
1000um
Cluster ID 1 1 1 2 2 3 3 3 3 3 3 4 4 4
B
Observed
Shuffle
Observed
Shuffle
3.1
2.7
2.6
2.4
3
5
10
Cells per cluster
C
Density (a.u.)
59
71
Mouse
Shuffled Mouse
Human
Shuffled Human
447
537
10
100
1000
10000
Cluster length (μm)
D
Matching
Non-matching
Human Rad: 250 500 750 1000 2000 2500 3000 6000 10,000
Mouse Rad: 50 100 150 200 400 500 600 1200 2000
Population demography vs shuffle (%)
More than shuffle
Less than shuffle
E
Outer Shell
Subtracted Core
Outer Shell
4000um
2000um
1000um
500um
Population demography vs shuffle (%)
100/0
500/0
200/100
1000/500
300/200
1500/1000
400/300
2000/1500
Shell / Core Radii

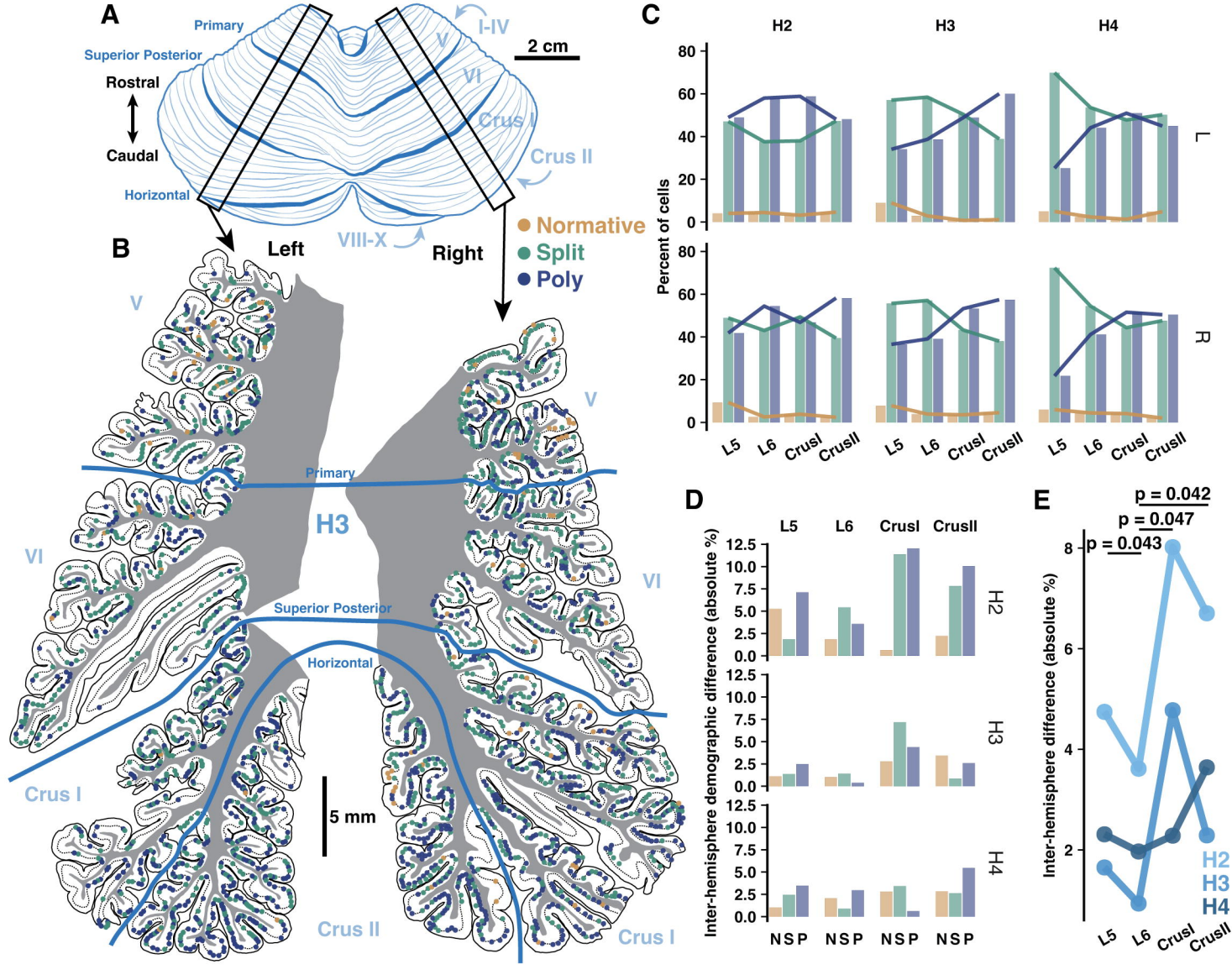
A
Primary
Superior Posterior
Rostral
Caudal
Horizontal
I-IV
V
VI
Crus I
Crus II
VIII-X
2 cm
Normative
Split
Poly
B
Left
Right
V
VI
Primary
H3
Superior Posterior
Horizontal
Crus I
Crus II
5 mm
C
H2
H3
H4
Percent of cells
L
R
L5
L6
CrusI
CrusII
D
Inter-hemisphere demographic difference (absolute %)
H2
H3
H4
N S P
E
p = 0.042
p = 0.047
p = 0.043
Inter-hemisphere difference (absolute %)
H2
H3
H4